2023

Optimizing Biomechanical models: Estimation of Muscle Tendon Parameters and Ankle Foot Orthosis Stiffness

Sepehr Ramezani
University of Central Florida

OPTIMIZING BIOMECHANICAL MODELS: ESTIMATION OF MUSCLE-TENDON PARAMETERS AND ANKLE FOOT ORTHOSIS STIFFNESS

by

SEPEHR RAMEZANI
B.S. University of Amirkabir, 2011

A dissertation submitted in partial fulfilment of the requirements
for the degree of Doctor of Philosophy of Mechanical Engineering
in the Department of Mechanical and Aerospace Engineering
in the College of Engineering and Computer Science
at the University of Central Florida
Orlando, Florida

Summer Term
2023

Major Professor: Hwan Choi

ABSTRACT

The complexity of the human musculoskeletal system presents challenges in accurately identifying its characteristics, particularly due to the presence of redundant actuators on a single joint. Non-invasive measures are necessary to overcome these challenges. Optimization algorithms have emerged as a crucial tool to advance subject-specific musculoskeletal modeling allows a more realistic representation of biomechanical behaviors, enhancing our understanding of human movement and enabling better clinical decision-making. Furthermore, optimization algorithms play a vital role in customizing rehabilitation and assistive devices, such as orthoses and prostheses. The current ankle-foot orthosis (AFO) stiffness measurement methods require bulky, complex designs, and often permanent modification of the AFO. To address this, we proposed the Ankle Assistive Device Stiffness (AADS) test method, which utilizes a simple design jig and motion capture system. In our method we employed a static optimization algorithm to estimate external forces and AFO torque, providing reliable stiffness quantification. The AADS test demonstrated high precision among different operators and trials, with an overall percent error within ±6%.

In the pursuit of accurately measuring muscle-tendon parameters, various techniques, including shear waves, have been utilized. However, these techniques often are invasive or lack the ability to provide quantitative measurements. In our second study, we introduced a noninvasive method for estimating passive muscle-tendon parameters (PMPs) in knee flexors/extensors and the Achilles tendon. We employed a direct collocated optimal control algorithm and evaluated the precision of the proposed method through simulation, replica leg experiments, and in-vivo experiments involving 10 subjects. The estimated range for tendon slack length was reported between 0.59 and 1.13, while the median of tendon stiffness was 421 KN/m. Muscle stiffness ranged between 473 N/m and 1200 N/m. The average root mean square error (RMSE) between experimentally collected joint kinematics and kinetics and forward dynamic verification was less than 0.56° and 12

mN.m/Kg, respectively.

To my Parents

ACKNOWLEDGMENTS

I am grateful to all who supported me in accomplishing my research to complete this dissertation. I would like to begin by expressing my greatest appreciation to my Ph.D. advisor, Prof. Hwan Choi, for giving me this opportunity to pursue my doctorate program under his supervision, to grow as a researcher, and to expand my knowledge. The experience that I have earned in his laboratory will guide me for many years and I am extremely appreciative of the guidance and mentorship that I have received. He was more than an advisor to me, and ever since I began my doctorate program, he has provided invaluable assistance and support to me, and I feel lucky to be among his students. I hope our scientific collaborations will continue throughout my career. I would also like to express my gratitude to the rest of my committee members, Dr. Qiushi Fu, Dr. Joon Hyuk Park, and Dr. Woo Hyoung Lee for their time to evaluate my research and for their constructive comments and discussions. Besides, I must appreciate Dr. Matt S. Stock their help in the completion of my research by providing experiment facilities.

TABLE OF CONTENTS

LIST OF FIGURES

LIST OF TABLES

CHAPTER 1: INTRODUCTION

In bio-mechanical system involving human movement and mechanical interactions, it requires careful consideration of multiple variables and constraints. Optimization algorithms offer a powerful toolset to navigate this complexity and identify solutions that maximize desired outcomes or minimize certain objective functions. Many problems can be naturally formulated as the optimization of a system's parameters and time-varying controls. The goal of optimization algorithm is typically to minimize a specific cost, such as, muscle activation, energy consumption, error between experimental and simulation and etc, while accounting for the dynamic of the system.

One of the primary areas where optimization algorithms have made significant contributions is in the field of rehabilitation and assistive devices such as prostheses and orthosis. One key benefit is the ability to customize and fine-tune these devices to meet the unique needs and preferences of each individual. Optimization algorithms allow clinicians and researchers to optimize various parameters, such as stiffness and mechanical properties to maximize comfort, stability, and functionality.

Ankle-foot orthosis (AFO) is an assistive device designed to provide support and alignment for individuals with neurological or physical impairments affecting their ankle and foot control [3]. Tuning the dorsiflexion stiffness of AFOs during the stance phase has been widely used to optimize their performance for individual users, leading to improvements in walking ability [4, 5]. To determine the optimal AFO stiffness, reliable measurement methods are necessary. Traditional AFO stiffness measurement techniques utilize fixtures, load cells, and potentiometers to capture torque, load, and deformation. In the first study, to overcome the existing limitations in AFO stiffness measurement, we propose the Ankle Assistive Device Stiffness (AADS) test. The Objective of this study is developing a reliable and repeatable method to measure the stiffness of the AFO

using a motion capture system instead of complex and dedicated equipment. By leveraging the existing resources commonly found in gait labs, we have developed an innovative technique using optimization algorithm that incorporates multiple axes to accurately assess AFO stiffness. Unlike conventional approaches that rely on bulky actuators, our method utilizes the operator as a source of bending force, resulting in a more compact and straightforward setup. This approach enables researchers and orthotists without specialized measurement devices to easily access AFO stiffness measurements. To validate the feasibility and precision of the AADS test, we conducted experiments using AFOs with known stiffness settings and compared the experimental results with the theoretically calculated AFO stiffness.

The other areas where optimization algorithms have made contributions is in musculoskeletal modeling. Musculoskeletal models simulate the interactions between muscles, bones, and joints to accurately represent human movement. These models are vital tools for studying human performance, predicting joint forces, and evaluating the effectiveness of therapeutic interventions. However, the measurement of subject-specific parameters such as muscle tendon parameters is necessary to model the human musculoskeletal. Moreover, individuals with movement disorders, such as stroke survivors and children with cerebral palsy, often exhibit altered muscle characteristics such muscle stiffness. Measurement of muscle passive parameters can be extend to evaluating PMPs in these specific populations, leading to enhanced treatment methods and better understanding of informing clinical decision-making. Hence muscle-tendon passive parameter such as muscle-tendon stiffness and tendon slack length have draw the attention.

The traditional approach to measuring musculotendon parameters involves the invasive removal of musculotendons from cadavers, followed by stretching them using a tensile testing machine [6]. An alternative method utilizes ultrasound imaging combined with motion capture to measure passive musculotendon parameters [7, 8]. More recently, shear waves have been employed to indirectly assess tissue stiffness [9–12]. However, these methods lack the ability to provide quan-

titative measurements of stiffness due to the discrepancy between sound units and mechanical force/displacement units.

Despite previous efforts to measure passive musculotendon parameters, several unresolved limitations persist. Noninvasive methods capable of accurately quantifying muscle-tendon stiffness, particularly in terms of passive parameters, are still lacking. Additionally, the absence of ground truth data for validation poses a significant challenge [6–12]. These limitations highlight the need for further advancements to address these challenges and enhance the accuracy and reliability of musculotendon parameter estimation methods.

In the second study, a novel noninvasive method was introduced to estimate passive musculotendon parameters, including tendon slack length (TSL), muscle stiffness (MS), and tendon stiffness (TS) in knee flexors/extensors. The objective of this study is measuring the stiffness accurately using a direct collocated optimal control optimization algorithm. The objective of the study was validated by examining the precision of the proposed method through three different techniques. The method can help to evaluate the efficacy of the surgery methods and suggests refinements to the treatment based on desired stiffness. These advancements offer promising prospects for accurately and noninvasively assessing musculotendon parameters, providing valuable insights into the biomechanics of human movement.

CHAPTER 2: A METHOD FOR QUANTIFYING STIFFNESS OF ANKLE-FOOT ORTHOSES THROUGH MOTION CAPTURE AND OPTIMIZATION ALGORITHM

This chapter has been published in open access journal of IEEE Access by Sepehr Ramezani [13] and Brian Brady and Hogene Kim and Michael K. Carroll and Hwan Choi "A Method for Quantifying Stiffness of Ankle-Foot Orthoses Through Motion Capture and Optimization Algorithm" in IEEE Access, vol. 10, pp. 58930-58937, 2022, doi: 10.1109/ACCESS.2022.3178701. The link for license is provided in appendix

Introduction

Ankle-foot orthosis (AFO) is an assistive device intended to support neurologically or physically impaired individuals who require assistance in controlling and aligning their ankle and foot [3]. Adjusting dorsiflexion stiffness during stance phase is a common method for tuning AFOs that can provide subject-specific improvements in walking [4,5]. It has been shown that properly prescribed AFOs can reduce the energy cost of walking [14,15], improve the gait pattern of the wearer [16–22] and provide stretching rehabilitation through gait [23–25]. Among many ways to tune the AFO to get the best outcomes, stiffness is one of the most commonly tuned parameters [26]. In current clinical practice, AFOs are prescribed largely by orthotist discretion rather than quantitively which makes the process subjective [27]. Vasiliauskaite et al. found that using a quantitative method to customize the mechanical properties of AFOs to specific user needs was advantageous over the traditional clinical practice [28].

To reach the optimal AFO stiffness we need reliable measurement methods. Typical AFO stiff-

ness measurement methods use fixtures that affix the AFO to the testing device, a load cell that measures the engaged or response of torque, load, and potentiometers that measure the deformation of AFO [29–32]. There are many types of AFOs such as hinged joint AFO, posterior leaf spring AFO, and AFO with adjustable stiffness mechanisms. The variance of designs can create complex joint moments as AFOs are being dorsiflexed, capturing six degrees of freedom response (three translational forces and three rotational moments on each axis of the Cartesian coordinates system) that cannot be fully captured with uni-axial loadcells.

Using multi-axis loadcells with custom designed fixtures can provide accurate AFO stiffness measurements by capturing the moment from complex shapes and mechanisms [5, 30, 33, 34]. However, fixation of the apparatus affects the deformation of the AFO and loading responses. As a result, there might be discrepancies between the measured AFO stiffness designed with specific fixtures and AFO stiffness experienced in normal use [30]. The loading methods of previous measurement techniques are either manual or automated. Although automated loading methods provide convenient and consistent loading input, this requires controls of actuators leading to operation complex. As a result, these limitations hinders other research lab from adopting these methods [5, 30, 31, 35–37].

Using commercial torque or load measurement tools such as a human dynamometer [38], an industrial robot arm [39], or a universal testing machine [40] enables measuring the AFO stiffness without custom measurement device fabrication. However, these devices still require specifically design testing jig to apply bending to measure the AFO stiffness. In addition to this, the robot arm and universal testing machines are not directly related to the walking assessments with AFO, so it would be challenging to access these modalities for the people who analyze walking with motion capture systems. Both custom design AFO stiffness measurement apparatus and commercial measurement tools employ specific actuators, such as a motor, a hydraulic cylinder, and loading weights that require specially designed fixtures for the actuators, leading to heavy, bulky, and ex-

pensive testing devices.

To address current measurement limitations, we are presenting an Ankle Assistive Device Stiffness (AADS) test for determining ankle stiffness of AFOs through the use of a motion capture system rather than a specifically designed, complex, and fixated system. Using equipment readily found in gait labs, we derived an innovative technique that considers forces and moments on multiple axes to accurately measure AFO stiffness. In addition, using operator as a source of bending force instead of bulky and heavy actuators enables equipment to be compact and straightforward. Thus, this method allows accessible AFO stiffness measurement for both researchers and orthotists who are not trained to use specifically designed or commercially avaialble measurement devices. To evaluate the feasibility and accuracy of the AADS test method, we tested AFOs with known stiffnesses to compare experimental results with theoretically calculated AFO stiffness.

Methods

AADS Test Jig Design

The shank and foot used in the test was a 3D printed replica model of the subject's leg. A hole was made in the shank to allow a 30 mm diameter pylon that is commonly used for lower limb prostheses to pass through vertically. The pylon creates a longer lever arm, reducing operator effort for higher stiffness AFOs. A ball and socket joint (CR-MO $1/2$" DR., Lexivon, Moorpark, CA) was used to connect the pylon to the foot (Fig. 2.1). The AADS test jig design can be downloaded at https://simtk.org/projects/foot-orthoses.

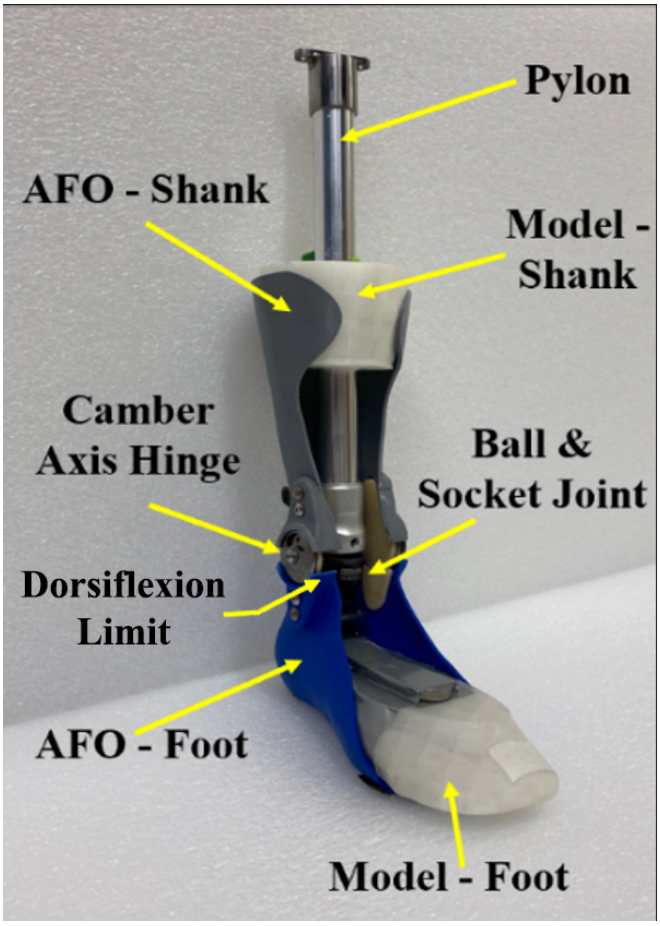

Figure 2.1: An overview of the AADS Test. Starting by applying force to an AFO on a force plate, the AFO bends around its center of rotation. Using motion capture marker trajectory, inverse kinematics was processed in OpenSim. The results from inverse kinematics were then used to find the AFO stiffness via static optimization algorithm.

Ankle-Foot Orthosis (AFO) Design

An individualized AFO, based on a 3D scan of a patient's leg, was created by the 3D CAD Software, Meshmixer (Autodesk, Mill Valley, CA). As seen in Fig 2.1, the hollowed leg scan was trimmed to the shape of an articulated off-the-shelf AFO. A Camber Axis Hinge (Model 750, Becker Orthopedic, Troy, MI) connected the foot and shank portion on the medial and lateral sides. Extended strut bars were created on the posterior of the AFO shell to allow a spring attach-

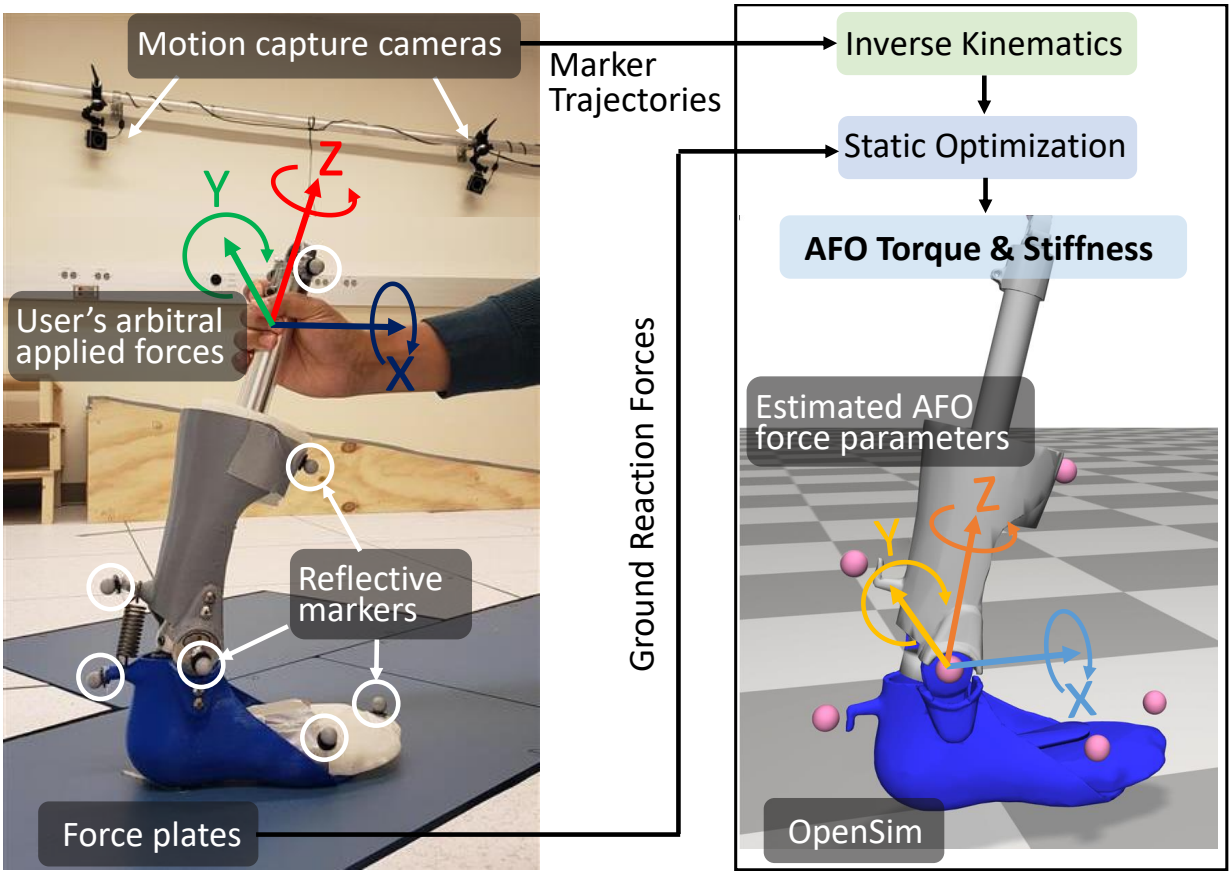

Figure 2.2: An overview of the AADS test. Starting by applying users' arbitral six degrees of freedom forces and moments to an AFO on a force plate, the AFO bends around its center of rotation. Using motion capture marker trajectory, inverse kinematics was processed in OpenSim. The results from inverse kinematics and experimentally obtained six degrees of freedom reaction forces and moments from the force plate were then used to find the AFO stiffness via static optimization algorithm.

ment to provide dorsiflexion resistance. With the designed model, the fuse deposition modeling 3D printer (Pro2, Raise3D, CA, U.S.) was used to print the AFO. The thickness of the AFO was set to 3.5mm, and 3D printed using Advanced Polylactic acid (APLA) with a 70% infill.

Testing

The trials for verifying AADS test performance, were conducted using twelve motion capture cameras (Vero, Vicon, UK) with a force plate (OptimaTM, AMTI, MA). From the motion capture cameras, marker trajectories on the AFO and AADS test jig were measured to identify the dorsiflexion angle of the AFO. The force plate was used to collect the ground reaction forces and moments in all three dimensions, as well as the center of pressure and angle measurements (Fig. 2.2). Reflective markers were placed following a modified Helen Hayes marker set [41]. Markers for the foot were placed on the AFO and leg replica in areas representative of the first and fifth metatarsal, middle cuneiform, and heel. Markers to represent the shank were placed at the equivalent location of the medial malleolus, the lateral malleolus, the anterior tibia, and the posterior tibia. The heel and posterior tibia markers were placed to track the displacement of the bottom and top of the spring respectively.

To start the trial, the AFO was placed on the force plate with the spring at the equilibrium position. Velcro was used to attach the foot to the force plate to prevent AFO heel lift and slipping. During the trial, the operators were instructed to push the AFO down, then return the AFO to the neutral position. The AFO has dorsiflexion stop limited to a maximum angle of 21° (Fig 2.3). Since the spring was not engaged at small AFO dorsiflexion angles, the toque of the AFO was obtained from the 5° dorsiflexion angle. To accurately determine the stiffness of the spring, torque out of range of minimum (less than 6°) and maximum AFO dorsiflexion angle (greater than 20°) were not considered for the stiffness calculations.

Three different springs were used to modify the AFO stiffness: 9,910 N/m (Spring 1), 15,600 N/m (Spring 2), 25,200 N/m (Spring 3). Each spring was randomly donned to the AFO and tested by four different operators, each running five trials. Each operator was given minimal instructions to ensure ease of use to future operators and validation of AFO stiffness repeatability in different

bending conditions. From the instructions, the operator was able to decide the AFO dorsiflexion bending speed, direction of force, and range of AFO dorsiflexion angle.

Modelling AADS Test in OpenSim

OpenSim, an opensource musculoskeletal analyses software, was used to derive AFO stiffness [42]. A 3D model of the AFO and AADS test jig from the computer-aided design were imported to OpenSim to create a model. The model was composed with one rotational degree of freedom on the sagittal plane of the ankle joint, and six degrees of freedom on the center of mass of the entire AFO and AADS test models. The distance from experimental reflective marker positions and virtual markers in OpenSim were monitored to verify accuracy of scaling. The maximum marker errors for bony landmarks were less than 2 cm and overall root mean square error of all markers were less than 1cm [43,44]. The moment of inertia and the center of mass for each AADS test jig segment and AFO segment was calculated by SolidWorks (SolidWorks, Dassault Systmes SE, France). Also, each AADS test jig and AFO segment's mass was measured with digital scale. These acquired moment of inertia, center of mass, and mass data were imported to the model in OpenSim.

Data Processing

Using OpenSim and the imported motion capture data from each trial, inverse kinematics was performed. Inverse kinematics calculated the AFO ankle joint angle by matching the experimental marker trajectories with the simulated marker set. To account for unknown external loads from the operator, static optimization (SOP) algorithm was employed [45]. SOP is designed to solve redundancy problems of human musculotendon dynamic systems. To customize SOP to AADS test analyses, three force and three torque actuators at the top of the shank model, and one coordinate

actuator at the ankle joint were added. SOP determined the minimum input controls for these actuators that matched experimental reaction forces and moments from the force plate considering AFO kinematic. Using the estimated AFO torque profile with dorsiflexion angle, linear fit was used to determine the level of AFO stiffness in the sagittal plane.

Validation of Results

The theoretical stiffness of the AFO was calculated to determine the validity of the results. During the trial, two markers were placed on the surface of the hooks (red circles in Fig. 2.3). Using the position of these markers, a virtual marker was put at the proximal part of the spring $T(x, y, z)$, and a marker was placed at the distal part of the spring $B(x, y, z)$ (green circles Fig. 2.3). The spring length SL, was calculated by:

$$|S_L| = \sqrt{(x_T - x_B)^2 + (y_T - y_B)^2 + (z_T - z_B)^2} \tag{2.1}$$

Having initial spring length (S_{L0}), the spring displacement (ΔS) is derived by following equation.

$$\Delta S = S_L - S_{L0} \tag{2.2}$$

Since we have used linear spring the force produced a spring is equal to:

$$F = \Delta S.k \tag{2.3}$$

The moment generated by spring, Ms, on the AFO ankle, was calculated by following equation.

$$M_s = F|AD| \tag{2.4}$$

Where $|\overrightarrow{AD}|$ is the normal distance between the ankle joint $A(x, y, z)$ and the line created by the T and B virtual markers. $\overrightarrow{AD}$ is connected to the line at point $D(x, y, z)$ at any given time. To find the position of point D, an unknown constant, q were multiplied to the line created by the spring (BT), which $0 \leq q \leq 1$:

$$\overrightarrow{AD} = \overrightarrow{AB} + q\overrightarrow{BT} \tag{2.5}$$

$\overrightarrow{AD}$ is perpendicular to the $\overrightarrow{BT}$ dot product between two vectors crossing at a 90° is equal to 0.

$$0 = \overrightarrow{BT} \cdot \overrightarrow{AD} \tag{2.6}$$

This was used to solve for the unknown variable, q:

$$\begin{aligned} 0 = (x_T - x_B)(x_B - x_A + q(x_T - x_B)) \\ + (y_T - y_B)(y_B - y_A + q(y_T - y_B)) \\ + (z_T - z_B)(z_B - z_A + q(z_T - z_B)) \end{aligned} \tag{2.7}$$

After q was found, it was substituted into the equations solving for (AD_x, AD_y, AD_z). The magnitude of this vector gives the moment arm, and was solved via:

$$|AD| = \sqrt{{AD_x}^2 + {AD_y}^2 + {AD_z}^2} \tag{2.8}$$

Using equation (2.4) and (2.8), AFO stiffness is then calculated by:

$$k = \frac{M_s}{\theta} \tag{2.9}$$

Where θ is the ankle angle from inverse kinematic. Although we have used linear spring, AFO stiffness showed some level of nonlinear behavior due to changes in moment arm. To introduce

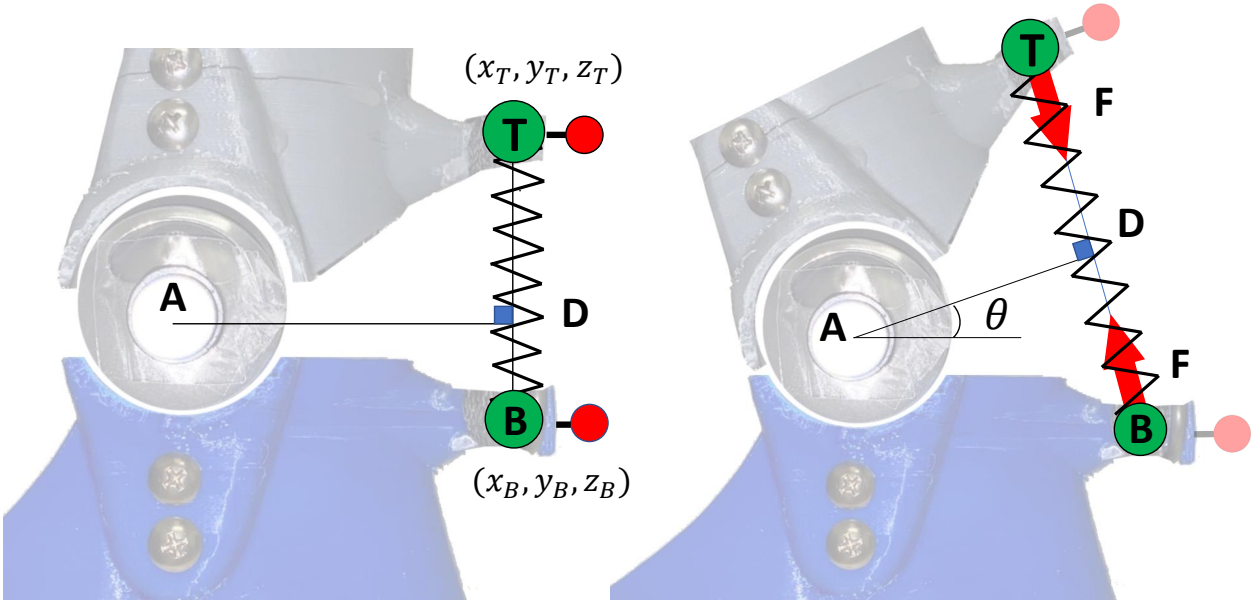

Figure 2.3: A labelled diagram demonstrates the positions of the center of AFO ankle joint, the proximal part T and distal part B of the spring. Point D is the shortest distance away from the center of AFO ankle joint and changes throughout the trial. The force vectors F and AFO dorsiflexion angle θ were used to calculate AFO torque.

a representative constant number for AFO stiffness, we fitted a line to the torque-angle plot. This method was employed for every trial, and the average value for all trials on one spring was used as the theoretical stiffness.

Statistical Analysis

A multi-factor analysis of variance (ANOVA) [46] was used to determine which factor (e.g. different users and different springs) contributed the greatest to the total error to assess the repeatability and reliability of the AADS test (Table 2). We defined different source of errors to verify which factor causes major error in accuracy of AFO stiffness estimation. Factors that likely caused the error are the different springs (Spring), the different operators (Operator), the different trials within

the same operator (Trial), and the effect of the different springs on each operator that determines how varying spring stiffness could affect operators AFO bending performance (Spring × Operator). We also evaluated other factors outside the main experiment variable conditions (Residual). For example, an operator with less strength could struggle to bend an AFO with a stiffer spring. F-value (F) and Type I error (Prob $>$ F) was calculated from the mean sum squared (MS), the partial sum squared (SS), and the degrees of freedom (DF) to evaluate how overall and each error source statistically impact the accuracy of estimated AFO stiffness with SOP.

Result

Each AFO bending trial starts at 5° dorsiflexion, the operators chose to bend the AFO angle with 15° - 27°, depending on the operator's discretion (Fig. 2.4). Both operator 1 and 2 bent AFO beyond the maximum dorsiflexion limit (21°) in all spring conditions. Operator 4 only exceeded AFO dorsi-flexion in spring 1 condition. According to the SOP results, Spring 1 had a maximum torque of 16 Nm, Spring 2 had a maximum torque of 25 Nm, Spring 3 had a maximum torque of 36 Nm.

In the Table2.1, the most compliant AFO stiffness case (Spring 1) had the smallest standard deviation (SD) out of the three springs. As the spring stiffness increased (Spring 2 and 3), the magnitude of the SD increased. The percent error of Spring 1 shows that the experimental stiffness value was 5.4% higher than the theoretical stiffness. As the stiffness of the spring increased, the percent error decreased in value. The experimental stiffness value of Spring 2 and 3 was 4.6% and 5.9% lower than the theoretical stiffness.

The F-value and the type I error values from multi-factor ANOVA demonstrates that the AADS test gives reliable and repetitive results regardless of different stiffness conditions, operator order,

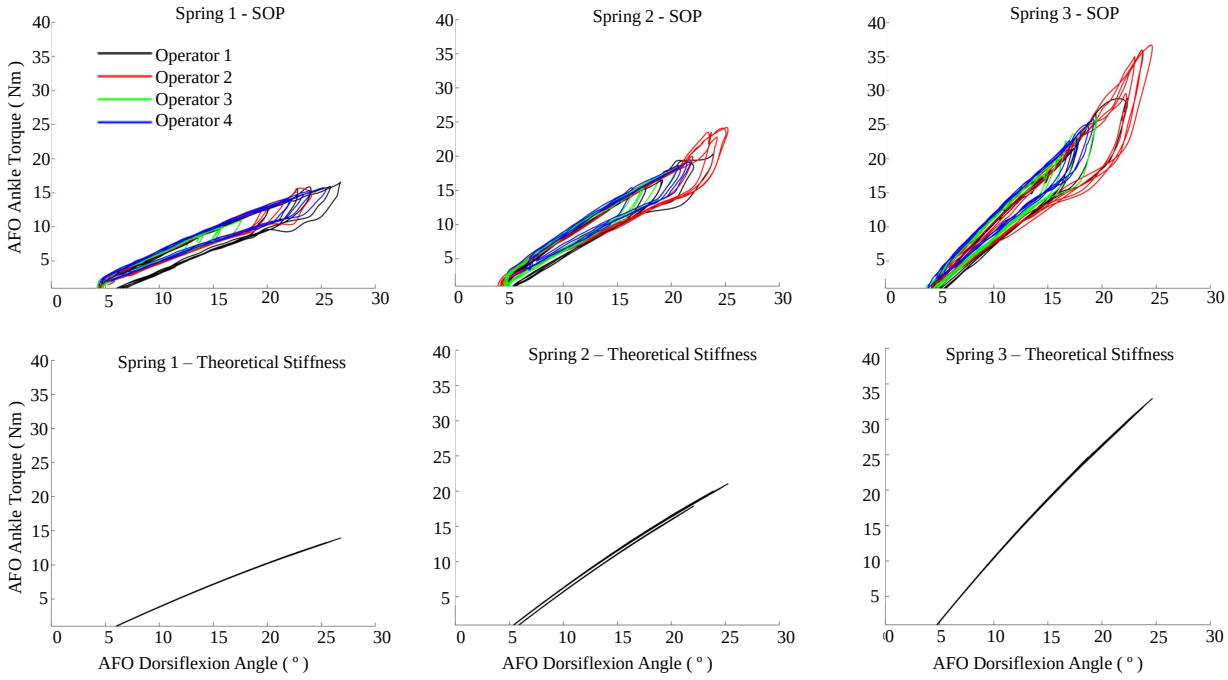

Figure 2.4: The graphs on the top show the plots from the static optimization results of different operators and multiple trials, while the charts on the bottom show the results from the theoretical calculations. For both the static optimization and theoretical graphs, all five trials of all four operators were plotted (20 trials per graph).

trial order, and each operators strength to control the AFO bending. Overall, there is no significant difference between estimated AFO stiffness from SOP and theoretically calculated AFO stiffness (Table 2.2).

Discussion:

The goal of the paper was to develop a novel method to determine the stiffness of an AFO. With the use of a force plate and motion capture cameras, the AADS test is quick, easy-to-use, compact, and an accessible method for those with a motion capture laboratory. The study showed the method is consistent across multiple trials and interchangeable between operators, suggesting the AADS test

Table 2.1: A table summarizing the calculated stiffness for each spring in second column. Column 3 shows the mean and Standard Deviation (SD) of the static optimization results for 20 trials between the four users and the distribution of the trial results. In column 4, the deviation of mean stiffness of SOP from the calculated stiffness value is given.

Spring	Theoretical Stiffness (Nm/°)	SOP Stiffness (Nm/°)	Percent Difference (%)
1	0.67	0.71±0.02	5.4
2	1.07	1.02±0.03	-4.6
3	1.69	1.59±0.04	-5.9

provides reliable AFO stiffness measures. While the theoretical AFO torque follows the same path on the plot when pushed down as when pulled up, there were hysteresis AFO torque curve from experimental results. The hysteresis curve was greater as spring stiffness and AFO dorsiflexion angle increases. This occurrence can be attributed to the AFO's design and material property. Since the AFO is made of APLA, it deforms as a large force is applied to it [47]. At higher stiffness, more force is required to bend the AFO, causing more deformation. The viscoelasticity material properties of APLA dissipates the applied force from the operator, resulting in a lower stiffness. The decrease in torque can also be attributed to the AFO returning to its equilibrium position, as this would not need operator input. This AFO shell deformation contributed to an increased stiffness curve (Fig. 2.4).

Table 2.2: A summarization of the Multi-Factor ANOVA test

Source	Partial SS	DF	MS	F	Prob>F
Model	0.187	15	0.012	14.36	0
Spring	0.175	2	0.087	100.31	0
Operator	0.006	3	0.002	2.13	0.111
Trial	0.001	4	0.000	0.35	0.845
Spring × Operator	0.006	6	0.001	1.17	0.34
Residual	0.038	44	0.001		0.001
Total	0.226	59	0.004		0.004

The model in OpenSim is a rigid body segment and does not account for deformation of AFO shells. Ideally, the distance of the spring is proportional to the AFO dorsiflexion, however, the deformation of the AFO shank shell allows greater AFO dorsiflexion because the markers on the pylon and AFO shell move more in the interior direction while the markers on the AFO foot is constrained with force plates. The theoretical force is however calculated via the markers close to the joint center, meaning deformation will not influence the force value as much as the angle. As a result, the estimated stiffness from SOP would underestimate ground reaction forces and moment values. This is shown by the difference between the rising and falling experimental difference growing as the spring stiffness increases. This is also supported by the percent error becoming more negative as the stiffness grows (Table 2.1). Future studies should use a more rigid AFO to avoid these deformation issues.

While deformation of AFO shells led to the negative percent error in Spring 2 & 3, friction of the hinge joint was the major error source in the least stiff Spring 1. When operators applied force to bend the AFO, this force was applied to the hinge joint and created friction. The AFO shell does not deform with the low stiffness spring (Spring 1) as much as it does with the stiffer springs. Thus, the resistance from the friction of the hinge joint may profoundly overestimate the results. The AFO shell deformation and friction of the hinge joint contributed to the theoretical and experimental stiffness errors, causing a relatively larger MS value for different springs compared with the other sources (Table 2.2). When the same operator used the AADS test, the results showed consistent stiffness values. The MS value shows negligible variations in the stiffness across trials suggesting that the result of estimated AFO stiffness with SOP is independent of operator strength, as long as they can bend the AFO to the desired angle. These outcomes show that the method is repeatable via the same operator, among the same AFO, or different AFOs.

When including the entire trial, the error stemming from the different operators is higher than the other sources of error. This was due to the different maximum angles the operators decided to

test. As operators bent the AFO, some users bent the AFO beyond 21° which was the maximum dorsiflexion angle for the AFO. As shown in the Fig. 2.2, the AFO stiffness of these cases had a greater stiffness slope compared with the AFO stiffness between 5° and 21°. This over bending of the AFO increased stiffness compared with the AFO stiffness attributed only to the spring. This led to greater discrepancies between operators, contributing to the F-value and type I error (Table 2.2).

As a previous study described, AFO stiffness varies depending on the alignment of the AFO rotational axis to the device [30]. This suggests that even if the same AFO is prescribed to each individual, the AFO applies a different stiffness due to inter-participant variability of rotational axes of the ankle joint on the sagittal plane and the frontal plane. Our AADS Test jig design is capable of adjusting the fore-aft and vertical position of the ball and socket joint on the Model-foot to match the wearer's ankle rotation joint center. This versatile jig design will enable the measurement of wearer-specific AFO stiffness.

The study only tested the viability of the AADS test with linear stiffness AFO model. Unlike our AFO model, actual AFOs that have nonlinear stiffness profile such as posterior leaf spring AFO, double-action AFO, or other AFOs may have intrinsic nonlinear stiffness in their design. Our algorithm matches the ground reaction data and ankle joint angles at the hinge joint of AADS by modulating the user's engaged forces and moments to find AFO torque using an optimization algorithm. This suggests that even if the AFO has a nonlinear stiffness profile, the optimization algorithm will find the solution of AFO torque and the user's engaged forces regardless of nonlinearity. In addition to this, our induced nonlinear stiffness profile from the AFO shell deformation at a greater bending angle supports our method's validity for AFO designs with nonlinear stiffness profiles.

The methodology also has the potential to measure the coronal and transverse stiffness of AFOs

with multiple degrees of freedom on the joint because the AADS accounts for three dimensional forces, moments and kinematics. This suggests that AADS test can be used to measure the AFO stiffness that has complex posterior leaf spring, off-the-shelf trimline geometries. However, this study only validated sagittal plane stiffness of AFO due to the specific design of AFO. Thus, future study will validate the other planes of motion and nonlinear stiffness profile AFO. Due to the versatility of test method, the AADS test also has the potential to evaluate the comprehensive stiffness of prostheses, knee braces, and other gait assisting devices.

Conclusion

An easy-to-use, quantitative method of determining AFO stiffness directly impacts patient care. A quantitative measure of AFO stiffness will allow for tracking patient AFO prescription as the patient's optimal AFO stiffness changes as their situation progresses. Having a procedure to measure the stiffness of the AFO can help orthotists prescribe and fabricate new AFOs for their patient. In addition, a record of the AFO stiffness will also be beneficial in refabrication when the AFO is damaged or requires resizing as the patient grows.

CHAPTER 3: MUSCLE TENDON PASSIVE PARAMETER ESTIMATION

Introduction

In primary method for measuring musculotendon parameters [6], musculotendons (MTs) are removed from a cadaver and are stretched using a tensile testing machine. The method is highly invasive and only can be used to measure the parameters of cadavers then it will be scaled based of the body segment length to create subject specific model [48]. This method may be inaccurate since muscle properties is not necessarily linearly related to limb length, especially in people with movement disabilities [48, 49].

Passive musculotendon parameters (PMPs) also was measured using ultrasound imaging combined with motion capture [7, 8]. The stiffness of Achilles tendon was measured by tracking the location of the prob attached to musculotendon junction related to the bone land mark during isometric task [50]. In other study the stiffness of medial gastrocnemius was directly measured by observing actual length changes in muscle fibers (fascicles) during short range stretching [51]. Recently shear waves ultrasonically have been used to indirectly quantify tissue stiffness [9–12]. Since the sound unit cannot directly correspond to the mechanical force and displacement unit, the acquired information cannot provide a quantitative number for stiffness. Additionally, these methods are most effective for mechanically unloaded scenarios unlike muscle-tendon tissues which in vivo exist under tension [52]. Thus, it is challenging to assess the overall tissue stiffness in non-homogeneous tissues like muscle because only small areas of tissue can be monitored with these methods.

Using an optimization algorithm to estimate the muscle parameters with a given experimental condition is an alternative method for identifying PMPs [53, 54]. In this method, an EMG-driven

optimization algorithm is employed to find the muscle optimal fiber length and tendon slack length for a musculoskeletal model to minimize error between experimental and simulation data [55]. Musculoskeletal models used in this method are usually based on scaled generic models [55] that use a Hill-type muscle model [56, 57] . Frederik et. al. [58], estimated active and passive muscle parameters of one participant from isokinetic and isometric exercises using an optimization algorithm. However, as the generated active muscle forces were dominant to generate net joint torque, passively induced joint torque from stretched muscle forces may not give proper information to estimated PMPs. As a result, this method may not provide reliable estimates of PMPs.

Most musculoskeletal simulation problems are the systems with adjustable parameters and time-varying controls that minimize a cost function subject to system dynamics [59]. The direct collocated method enforces the system dynamics to match the derivative of the system's differential equations using the states' derivatives [60]. Since this method can solve various cost functions with multiple model parameters, it has been used in estimating various parameters in different tasks such as motion tracking [61, 62], motion prediction [63–65], muscle properties estimation [66], and assistive device parameter optimization [67]. OpenSim Musculoskeletal Optimal Control (Moco) [59], is an opensource software toolkit for solving optimal control problems combined with OpenSim. This is capable of customizing muskoloeskeletal models and cost functions based on the given dynamic tasks [68].

Despite efforts made in previous studies to measure passive musculotendon parameters (PMPs), several limitations remain unresolved. Specifically, there is a lack of noninvasive methods capable of quantitatively assessing muscle-tendon stiffness, particularly in terms of passive parameters. Furthermore, the algorithms utilized in previous research are not capable of considering the entire system that consists of multiple complex constraint functions leading to the estimated outcomes may not fully represents the actual muscle parameters. Another critical issue is the absence of validation due to the absence of ground truth data. These limitations underscore the need for

further advancements to address these challenges and improve the accuracy and reliability of PMP estimation methods.

Hence, we introduced a noninvasive method to estimate PMP's including tendon slack length (TSL), muscle stiffness (MS) and tendon stiffness (TS) of knee flexors/extensors using a direct collocated optimal control algorithm in Moco. Additionally, three different techniques were employed to evaluate the precision of the proposed method.

Materials and Methods

In this study healthy adults were recruited to find their subject specific muscle tendon parameters. As these parameters are not directly measurable in vivo, we employed 3 different methods to verify our algorithm.The procedure for each method is illustrated in figure 3.1 with distinct blocks. The details of these blocks will be explained later.

In the In-Vivo method torque and angle data obtained from experiments were utilized by Optimazation algorithm to find the PMPs of the human leg model. The resulting optimal parameters were then applied to a scaled generic model to create a subject-specific musculotendon model. Forward dynamics was subsequently conducted on the subject-specific model, with the experimental torque serving as input and the motion generated by forward dynamics was compared with the experimental joint motion to evaluate the accuracy of the model.

In the fully simulation method, we generated synthetic torque data for the parameter optimization algorithm instead of using real-world data that may contain artifact signals. To achieve this, A musculoskeletal model was used in place of an actual human, and a torque estimation algorithm was employed to determine the best torque profile for generating isokinetic motion. Following this, the estimated torque was fed into the optimization process to determine the MPM of the generic

model. Prior to running the parameter optimization, we randomly altered the musculoskeletal model's PMPs to ensure the optimization was functioning correctly. Since the estimated torque is obtained from the musculoskeletal model and the true parameters are available, the results of the parameter optimization can be directly assessed. Moreover, forward dynamics similar to the previous method were used for verification purposes.

In the bio-inspired leg method, a simplified version of the human leg was constructed to replicate the leg's structure, joints, and muscles. The experiment was conducted on the mechanism instead of a human subject, and the collected torque and motion data were used as input for the parameter optimization algorithm to determine the PMP's of the mechanism. Unlike the fully simulated method, the experimental uncertainties are considered in this method. However, since linear springs with predefined stiffness were used in mechanism to resemble the human muscle, the actual values of PMP's were still accessible. This allows for comparison of the optimal parameters with their actual value, as well as for running forward dynamic evaluation to verify the results.

In-vivo

In this study, 10 individuals (5 males and 5 females with average age: 24.9 ± 5 height: $169.6 \pm 11 cm$ weight: $70.5 \pm 16 kg$) with no history of any musculoskeletal or neurological disorders were recruited to perform 2 different sets of involuntary knee flexion and ankle plantar flexion. All subjects provided informed consent before participating, and the testing protocol was approved by the University of Central Florida Institutional Review Board. To ensure that the discrepancy between the simulation and experimental results is not significant, a paired t-test was conducted Table 3.1. The assumption was that the model's accuracy would be within 2 %, with a standard deviation of the differences between the model and participants ranging between 0.5 % and 2 %. Based on these values, effect sizes of 4, 2, and 1 were obtained. A sample size of five data pairs

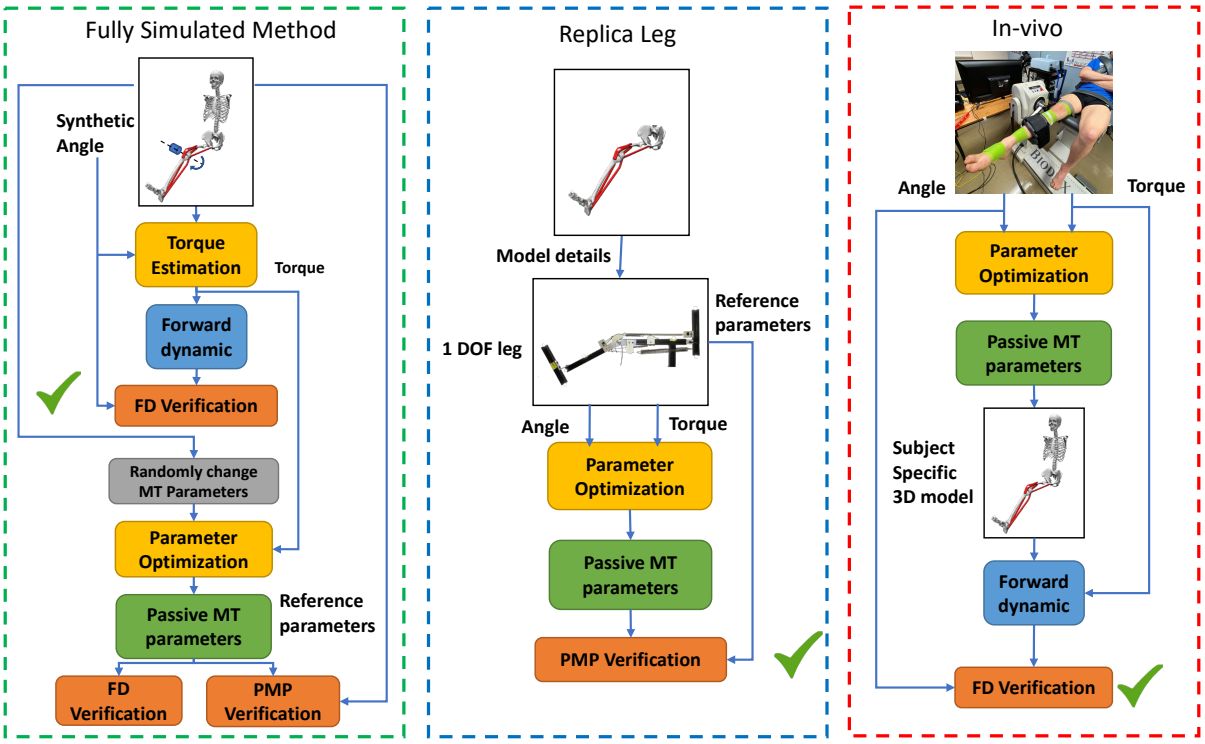

Figure 3.1: A comprehensive overview of the various workflows to verify and validate the proposed optimization algorithm, with yellow blocks depicting torque estimation and optimal parameter determination, blue and green blocks showing the results of parameter and forward dynamics, and orange blocks representing the various evaluation methods employed.

(number of participants) was determined to be sufficient to achieve more than 80 % power to reject the null hypothesis of zero effect size when the population effect size is 2, and the significance level (alpha) is 0.05, using a two-sided paired t-test.

The Table 3.2 is a summary of their relevant demographic information.

In the knee flexion setup, we positioned the subjects on a human dynamometer (System4 Pro, Biodex Medical Systems, NY) with their left knee fully extended in different hip angles. The shank was constrained with the jig of the dynamometer to enable knee flexion and the hip joint was adjusted with 90, 55, and 15° with the seatback of the human dynamometer. We unlocked

Table 3.1: Estimated sample size for a two-sample paired-means test Paired t test

alpha	power	N	delta	d0	sd_d	
0.05	0.8	3	4	0	2	0.5
0.05	0.8	5	2	0	2	1
0.05	0.8	10	1	0	2	2

Table 3.2: Demographic Information of 10 Participants

Subject	Gender	Age	Height (cm)	Weight (kg)	Leg Length (cm)	Thigh CIR (cm)	Shank CIR (cm)
1	M	29	160	56.7	80.5	45	31
2	F	24	157.4	54.4	76	56.5	36
3	F	19	160.2	52.1	79	50.8	33
4	M	33	185	94	93.4	61.2	45
5	F	23	170.2	65.7	82.55	54.6	37.4
6	M	28	167.6	75	75.56	54.6	35
7	M	20	190.5	95	96	63	40.5
8	F	19	172.7	81.6	83.8	63.5	39.4
9	M	23	172	76.6	89.5	51.4	35.5
10	F	31	161	54	78	53.97	32.38
Total		24.9±5	169.6±11	70.5±16	83.4±7.2	55.4±5.8	36.5±4.2

the dynamometer and let participants perform involuntary knee flexion at a slow constant speed (5 $^\circ/s$) to eliminate the induced muscle force from fast muscle stretch velocity [56]. The foot was unconstrained, allowing the ankle joint to rotate freely, thereby preventing the tension on the biarticular gastrocnemius muscle and minimizing its impact on the net torque during knee flexion sets.

In the ankle plantarflexion setup, the foot was constrained to the dynamometer using an ankle joint sagittal plane motion jig. The trial began with the ankle in a fully dorsiflexed position while the shank was horizontally constrained. Then, involuntary slow ankle plantarflexion with a 5 $^\circ/s$ speed was performed at different fixed knee angles (0, 45, and 90°) to differentiate the induced

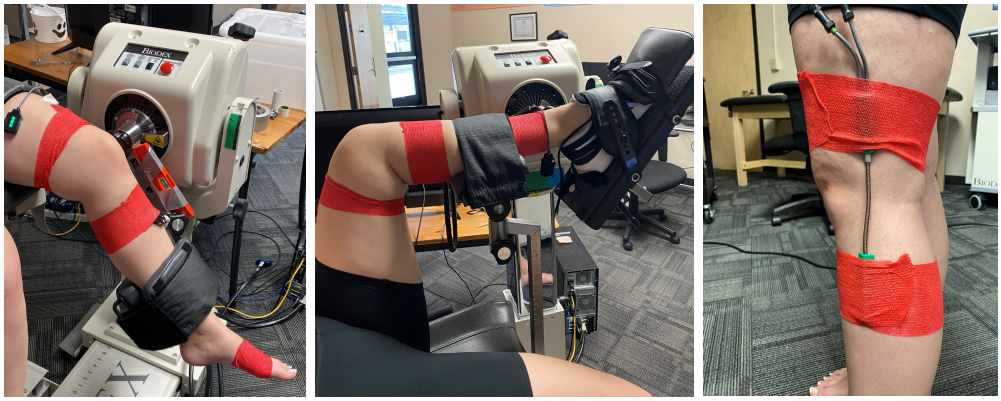

Figure 3.2: Experimental setup; left picture: dynamometer setup for knee motion, the middle picture: the setup for ankle motion, and the right picture: goniometer placement.

ankle torque from the gastrocnemius muscle.

Participants were instructed to remain relaxed during the test to avoid any unintended muscle activation, which could result in a jump in the torque signal. We monitored the torque signal to detect any such jumps, and any trials in which muscle activation occurred were discarded and repeated. The net torque generated by knee flexors, extensors, shank segment mass, and jig mass was recorded with the dynamometer. The knee and hip angles are recorded with electric goniometers.(Avanti wireless, Delsys, MA).

To compensate for the gravity effect on the jig to identify the net knee torque that is only induced by muscle stretch and human body segment mass, we measured the Biodex arm's length and weight. The human dynamometer experiment was conducted at a data collection rate of 100 Hz. This study focuses on primary muscles that dominate generating net knee and ankle joint torque. The target muscles in this study are: the biceps femoris long head (bflh), the biceps femoris short head (bfsh), the gastrocnemius lateralis (gaslat), the gastrocnemius medialis (gasmed), soleus, the semimembranosus (esmimem), the semitendinosus (semiten), the vastus intermedius (vasint), the vastus lateralis (vaslat), the vastus medialis (vasmed), and the rectus femoris (recfem). We made an

assumption that all muscles, except for the calf muscles, had small and rigid tendons. Therefore, in the optimization process, we focused only on the muscle stiffness of these muscles. However, the Achilles tendon which is the thickest and longest tendon in the human body [69] was taken into account because the Achilles tendon plays an important role in energy-efficient walking by storing and releasing energy.

Musculoskeletal model

We used a generic musculoskeletal model developed by Rajagoapl et al. [70]. In the Rajagopal model, we used modified Hill type musculotendon model proposed by Degoote et al. [66]. To scale the generic model, we measured various distances of each participant: thigh (greater trochanter to lateral epicondyle), shank (fibula head to lateral malleolus), hip (left to right anterior superior iliac spine), and foot (calcaneus to the tuberosity of fifth metatarsal). These measurements were used to determine the appropriate ratio between the generic model and the subject model. All model's coordinates have been removed/locked except for the left hip, knee and ankle to reduce the complexity and the computational time. The musculoskeletal model was placed in a seated position, resembling the posture of the human subject in the experiment 3.4. All muscles were deactivated to account for joints' torque derived solely from passive musculotendon forces and gravity.

Each muscle in the model was represented as a Hill-type muscle-tendon unit [57], consisting of an active element with a parallel elastic element that accounts for a muscle and a series elastic element that accounts for a tendon.(Figure3.3)

This model uses 4 different characteristic curves to calculate muscle force from muscle activation: an active muscle fiber force-length curve (f_{act}), a passive muscle fiber force-length curve f_{pas}, a muscle force-velocity curve f_v, and a tendon force-length curve f_T. The overall mathematical

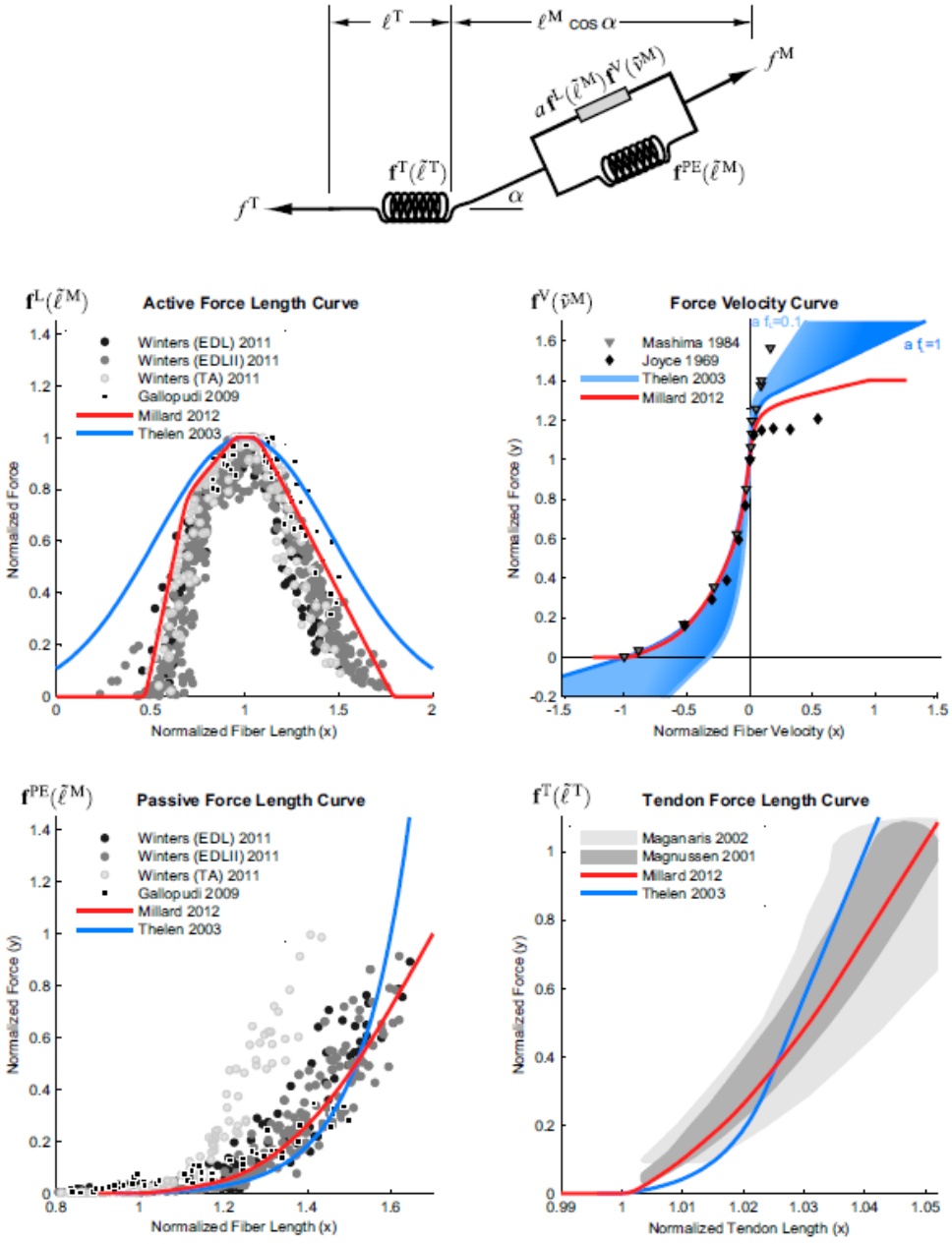

Figure 3.3: Hill-type model scheme including tendon fiber model [1]

model is:

$$F_M^0\left(af_{act}\left(\widetilde{l}_M\right)f_v(\widetilde{v}_M)+f_{pas}\left(\widetilde{l}_M\right)\right)\cos\left(\alpha\right)-F_M^0 f_T\left(\widetilde{l}_T\right)=0 \tag{3.1}$$

Where α and a are pennation angle and activation respectively and the maximum muscle force is equal to F_M^0 at a length of L_M^0. The tilde is used to denote forces, velocities, muscle lengths, and tendon lengths are normalized by F_M^0 (maximum isometric force), V^{max} (maximum eccentric velocity), L_M^0 (optimal fiber length), and L_T^s (tendon slack length) respectively.

Winter [6] and Gollapudi [71] collected experimental data explaining the active and passive muscle behavior and Magnusson et al. [72] and Maganar et al. [7] have examined the tendon force-length curve. Later on, Thelen. et. al. [73] and Millard et. al. [1] introduced modified mathematic formula to represent experimental data that were collected from the other previous studies (Figure 3.4). Degroote. et. al. [66] developed a new formulation to better describe muscle dynamics based on Thelen model. Since we only focused on the passive part of the muscle in a quasi-static motion, in the equation 3.1 active part of the muscle (f_{act}) as well as force velocity function (f_V) was ignored and be simplified as:

$$F_M^0\left(\left(f_{pas}\left(\widetilde{l}_M\right)\right)\cos\left(\alpha\right)-f_T\left(\widetilde{l}_T\right)\right)=0 \tag{3.2}$$

The formulation for the passive fiber force curve is :

$$f_{pas}=\frac{e^{\left(k^{PE}.\left(\frac{\bar{l}_M-1}{\varepsilon_0}\right)\right)}-b}{e^{k^{PE}}-b} \tag{3.3}$$

Where the f_{pas} is the normalized passive muscle force, k^{PE} is an exponential factor and considered [66] as constant value equal to 4. $\bar{l}_M$ is the fiber length normalized by the optimal fiber length and ε_0 is the passive muscle strain encountered at the maximum isometric force and can be set differently for different people. In the Thelen model, b is equal to 1, while in OpenSim developer modified the

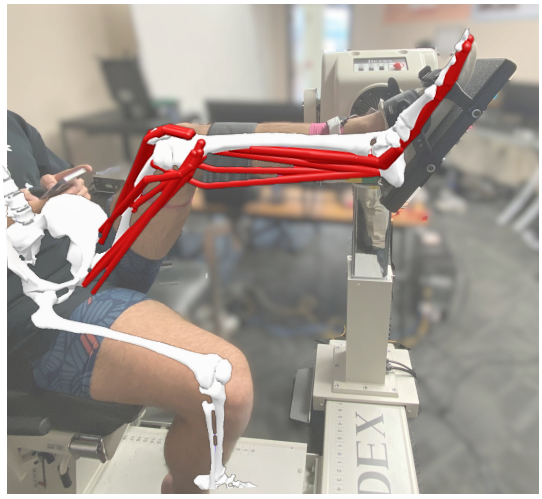

Figure 3.4: Musculoskeletal model seated in postures similar to human body

Degroote model to avoid negative force produced within allowed range by following equation [59]:

$$b = e^{\left(k^{PE}.\left(\frac{l^M_{min}-1}{\varepsilon_0}\right)\right)} \tag{3.4}$$

Tendon force is expressed as the following:

$$f_T = c_1 e^{\left(m_{kt}.\left(\bar{l}^T - c_2\right)\right)} - c_3 \tag{3.5}$$

Where $c_1,\ c_2,\ c_3$ are constants equal to 0.2, 1, and 0.2 respectively. $\bar{L}_T$ is the tendon length normalized by tendon slack length (L^s_T). m_{kt} is an exponential factor calculated by:

$$m_{kt} = \frac{\ln\left(\frac{1+C_3}{C_1}\right)}{1 + \varepsilon_{T0} - C_2} \tag{3.6}$$

Where ε_{T0} is tendon strain at the point that maximum normalized tendon force is created

Optimization

Simulations of human movement can be classified based on whether the motion is prescribed based on available data or predicted through the simulation process [59]. Prescribing the motion involves utilizing musculoskeletal models to estimate unmeasured quantities, such as muscle-level energy consumption or unknown parameters of the model [74–77]. On the other hand, motion prediction aims to estimate kinematic of model facilitating the design of clinical interventions, such as identifying gait trajectory of individuals with muscle weakness or developing prostheses for amputees [78–80]. User

Musculoskeletal simulation problems typically involve optimizing a system's parameters and time-varying controls to minimize a specific cost, such as energy consumption. These optimization problems are formulated as differential-algebraic equations that describe the system dynamics. Two primary approaches have been developed to solve these complex differential-algebraic equations: single shooting and direct collocation methods [81]. These methods aim to find the optimal solution by iteratively adjusting the system's parameters and controls.

In single shooting, the control strategy is initially selected, and then the states are integrated forward in time [78]. The optimizer aims to minimize a specific cost while adhering to equality constraints imposed at the end of the interval. In single shooting, the constraint relies on the control applied up to that point, and any alteration in the control policy affects the final error. Additionally, since integration spans the entire time domain, errors can accumulate, and the discrepancy at the end is influenced by the entire control policy. A major drawback of the single shooting method is the absence of assurance that the intermediate controllers iterated by the optimizer result in stable performance. It is possible that for certain control choices, the states may become infinite. Multiple shooting mitigates some of these concerns. In multiple shooting [82], the control policy is disctrzed as a piecewise linear (or constant) policy and discretize the states at these points. We

integrate from the beginning of the interval to the end and enforce the condition that the states at the end of the interval serve as the initial values for the next interval. This approach yields good convergence because each discretization step captures the impact of changing control inputs through a single defect. However, the optimization process is slow due to the numerical integration of states from the start to the end of the interval. Direct collocation methods have been developed specifically to address these challenges.

Direct collocation is an extremely potent technique for nonlinear optimization. It involves approximating the state and control variables using piecewise continuous polynomials and leveraging the properties of these polynomials to simplify the integration calculations involved. By converting the integration and other calculations into algebraic equations, the computation time for these parameters is significantly reduced. In direct collocation, the constraints on the system dynamics are imposed on intermediate points referred to as collocation points. The optimal solution is required to satisfy the optimality conditions solely at these intermediate points. The concept of direct collocation is visually depicted in the figure below.

A straightforward implementation of the direct collocation algorithm can be outlined as follows. Firstly, the control is approximated using a piecewise continuous linear function. Next, the states are approximated using piecewise continuous cubic functions, ensuring that the values at each discretization point (knot) match the corresponding state values, and the derivatives match the derivatives obtained from the system dynamics. It's worth noting that once the states and derivatives at the knot points are determined, the cubic function between the knots is completely defined. As a result, the intermediate values can only be modified by altering the state or derivative (through control). Finally, the condition is enforced that the derivative of the piecewise continuous cubic function must be equal to the state derivative calculated based on the system dynamics.

The direct collocation method offers several advantages over the single shooting method, includ-

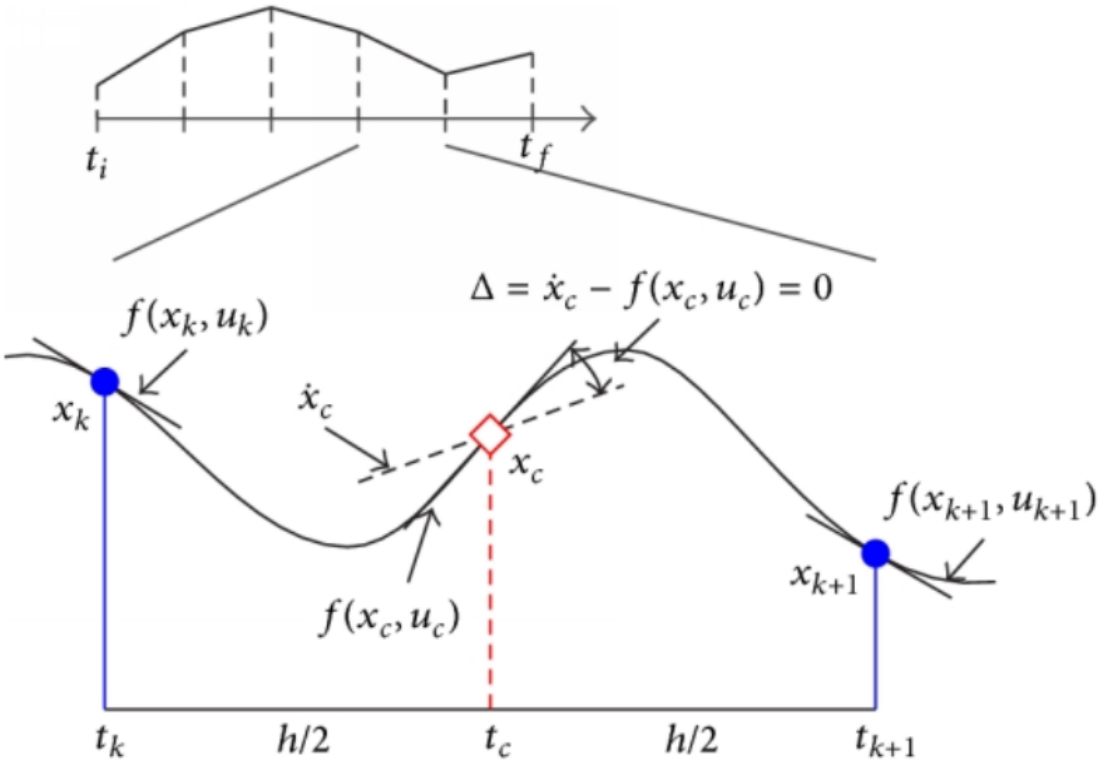

Figure 3.5: Direct collocation's core concept: Minimizing the discrepancy between state derivatives obtained from dynamics and those obtained through polynomial differentiations. [2]

ing its computational speed and elimination of the need to reduce the number of variables in the problem, as commonly required in single shooting. However, implementing direct collocation can be challenging since the convergence relies on the specific details of the problem formulation. To address the complexities of implementing direct collocation in biomechanics problems, we utilized Moco to complement the direct collocation method and estimate muscle-tendon parameters.

Torque Estimation

The human dynamometer controls motor torque to enable constant joint rotation speeds with varying net biological joint torque. To emulate the dynamometer in OpenSim, we generated a virtual actuator and placed on the musculoskeletal model similar to the experimental setup. To control the torque on the virtual actuator, the MOCO_track [59] optimization algorithm was used to minimize the difference between the desired and simulated joint kinematics, while the square of the actuator's control signal is forced to be minimized. Since all muscles are deactivated during isokinetic motion, the passive forces and gravity are the only sources of torque and MOCO finds the best torque profile to produce the desired motion while considering the system's dynamic. The cost function for this optimization is given by:

$$min\left(\int_{t_i}^{t_f}\sum_{s\in S}\omega_s \parallel x_s\left(t\right)-x_e(t)\parallel^2 dt+\int_{t_i}^{t_f}\sum_{c\in C}\omega_c \parallel u_c(t)\parallel^2\right) \tag{3.7}$$

Where t_i and t_f are the initial and final time of the phase. C and S are set of control and state variables which were being tracked. ω_c and ω_s The weight for actuator control signal and state terms in the objective function. $u_c(t)$ is the actuator control signal (input) which has the linear relation with out put torque by defining it's optimal force as 100. $x_m\left(t\right)$ represents the states of system including position and velocity of coordinates. And lastly $x_e(t)$ represents the reference data. the first term of the cost function guarantees minimize the error between model states and desired motion while second terms is a penalty term for activation of the actuator to find the efficient solution.

Musculotendon Passive Parameter optimization

The objective of the optimization algorithm is to determine the tendon slack length ($\bar{L}T$) for all muscles, as well as the parameter ε_0, which is associated with muscle stiffness, for knee flex-

ors/extensors excluding calf muscles. Additionally, the parameter $\varepsilon T0$, which corresponds to tendon stiffness is estimated for calf muscles. All other parameters in equations 3.2 to 3.6 are obtained from the scaled generic model. During the optimization, we restrict the parameters to certain boundaries to help the optimizer find the solution efficiently using the range of values that were experimentally collected from the previous studies [7, 83–87]. If a muscle is compressed beyond its slack length it will be buckled and equations 3.3 and 3.5 will no longer explain the muscle behavior. To avoid buckling during optimization, we calculated the muscle length in a full range of motion of hip, knee, and ankle joints to find the minimum length of muscles. From the calculated minimum length of the muscle, we assigned the upper bound of TSL while we use 60 % of the default value as the lower bound [70].

Either Estimated torque from torque optimization chapter or experimental data from human dynamometer was applied to the knee and ankle joint to enable isokinetic exercise. In this setup, the optimization algorithm in Moco estimated the PMPs that allow the virtual actuator on the knee and ankle joint motion to follow the reference motion in the presence of passive forces from muscles and gravity. Using MOCO_track, the states of knee and ankle joint kinematics and external torque will be tracked while PMPs were allocated from the optimization while the muscle activities are disabled. The cost function of the optimization is comprised of two terms. The first term of the cost function is the error between the experimentally collected joint kinematics (i.e., joint angles and isokinetic low speed knee flexion or ankle plantarflexion velocity) and the musculoskeletal model's joint kinematics. The second term of the cost function is tracking the virtual actuator's signal control. Since the virtual actuator signal control is linearly related to the external torque, tracking the actuator control is equivalent to tracking the external torque. Therefore, the second term of the cost function represents the error between the torque generated by the actuator in model and the reference torque. Following equation describes the total cost function.

$$min\left(\int_{t_i}^{t_f}\sum_{s\in S}\omega_s \parallel x_s(t) - x_e(t) \parallel^2 dt + \int_{t_i}^{t_f}\sum_{c\in C}\omega_c \parallel u_c(t) - x_{e_c}(t) \parallel^2 dt\right) \tag{3.8}$$

Where all the parameters are similar to equation 3.7 plus the $x_e(t)$ is represents the reference actuator input data.

Replica leg

To comprehensively evaluate the musculotendon parameter outcomes from the optimization algorithm, a physical model was developed that replicates the Rajagopal model's lower limb segments. As the experiment only considers the passive forces from the muscle and tendon and these models are comparable with mechanical springs [88], we used mechanical springs for each musculotendon. The actual value of springs' stiffness and the stiffness estimated by the optimization algorithm were compared to validate the algorithm. The replica leg is carefully designed to closely resemble the structure of a human leg, including the joints, body segments, muscle pathways, and muscle insertions.

Fabrication

The replica is comprised of 4 aluminum profiles that replicate a hip-to-foot bone structure (Figure 6) designed and assembled in SolidWork first. Each profile represents a body segment and is positioned so the hip sits horizontally and connects to the femur through a locking pivot joint. This joint is also used to represent the ankle joint (between the tibia and foot bodies) with a design that allowing for replication of both joints' full range of motion. The end of the femur is connected to the tibia via a knee joint which is the series of custom-made brackets that allows for the attachment of a torque sensor (DYJN-104, ATO, CA) between them to measure the joint's torque (the knee's

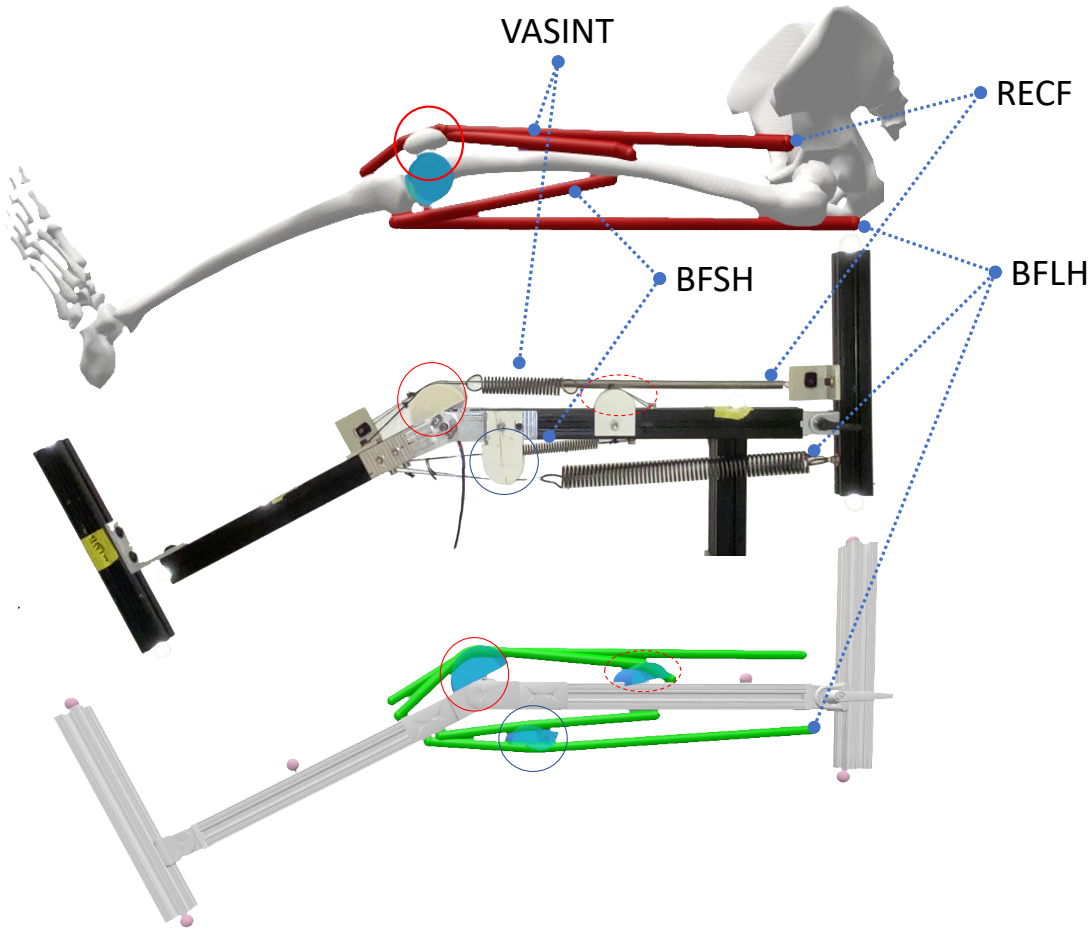

Figure 3.6: Overall design of leg mechanism (top), fabricated leg mechanism (Middle) 3D model in OpenSim (Bottom)

torque). The torque sensor used in this study measures torque in the mono-direction (rotation around knee joint), and any external load or torque applied in other axes can result in artifact signals. To address this limitation, knee joint is designed in a way that the sensor experiences torque in only one direction and minimizes the risk of any external factors. Also, we fixed the tight segment of the replica of leg on the ground to replicate the human seating positioning on the dynamometer. To replicate the muscle pathway of the Rajagopal model we designed wrapping

objects. Using Wrapping object geometric information from generic model we designed it in SolidWorks and 3D printed (Rise3D, Irvine, CA) cylinders with the same information. Also, Some of the springs were thick and cause collusion with other springs, considering this, extra wrapping objects added to prevent this conflict. Knowing that the aluminum profile does not consider the natural shape of the bone, we used bracket for the attachment point between frame and springs to roughly follows the muscle insertion points.

We used the equation 3.16 to calculate the average stiffness for four muscles: BFLH, BFSH, VASINT, RECF. Due to the strength restriction of wires and brackets that connect muscles to the frame selected, we choose springs close to a tenth of these average stiffness. Each spring is attached with minimal stretch at its shortest configuration, for example when attaching the recfem muscle, as it is a biarticulate muscle, the hip is angled at maximum flexion and the knee was fully extended so that the muscle can be fixed to the frame. Springs were labeled with names that correspond to the human knee flexors and extensors including the biceps femoris long head (BFLH), the biceps femoris short head (BFSH), the vastus intermedius (VASINT), and the rectus femoris (RECF) (Figure3.6).

Model

To implement the optimization algorithm, we made the exact model of replica leg in OpenSim. The segments designed in SolidWorks are imported into the OpenSim with their center of mass and moment inertia. We used the PinJoint() function in OpenSim for all coordinates however hip and ankle were locked during the optimization and knee only can rotate from full 0° to 90°. To model the linear spring used in the experiment, a PathSpring() function was used, which allows for defining the pathway of the actuator using insertion points and wrapping objects. Nine virtural markers were attached to key points on the aluminum profiles similar to the bonly landmarks on

the human body including the intersection of springs and bodies, the center of wrapping objects, and joint centers to record their relative positions. This data was then used in OpenSim to ensure the accuracy of the model dimension and joint angles.

Replica leg experiment

The knee joint of replica leg was adjusted to different angles with a fixed increment of 8° by locking the joint. A total of 12 trials were conducted for each of the for hip 90°. During each trial, the torque sensor was used to record the torque generated by the spring and the weight of the shank, while the motion capture system was used to measure the angle of the knee. Nine reflective markers (Figure 3.7) were placed on key points aligned with virtual marker position in OpenSim. Inverse kinematics was used to calculate the angles of the hip and knee. The ankle joint was fixed at 90° for all trials and hip was setup in 90° (perpendicular to thigh) while knee was from 0 (fully extended) to 90° with increment with 8° ((Figure 3.7). The recorded torque and angles were employed by the optimization algorithm to determine the stiffness and the resting length (the length at which the spring does not produce any forces) of each spring. The same optimization algorithm introduced in previous section was presented to estimate the parameters of the replica leg model with the goal of reducing the error between the experimental and simulation torque and angle.

Forward Dynamics Evaluation

A forward dynamic was performed to evaluate optimization outcomes for all three verification methods including fully simulation, replica leg and in-vivo. In the forward dynamics, the torque serves as an input of musculoskeletal model with optimized parameters. The motion generated by the forward dynamic was compared with the experimental joint motion to evaluate the accuracy of

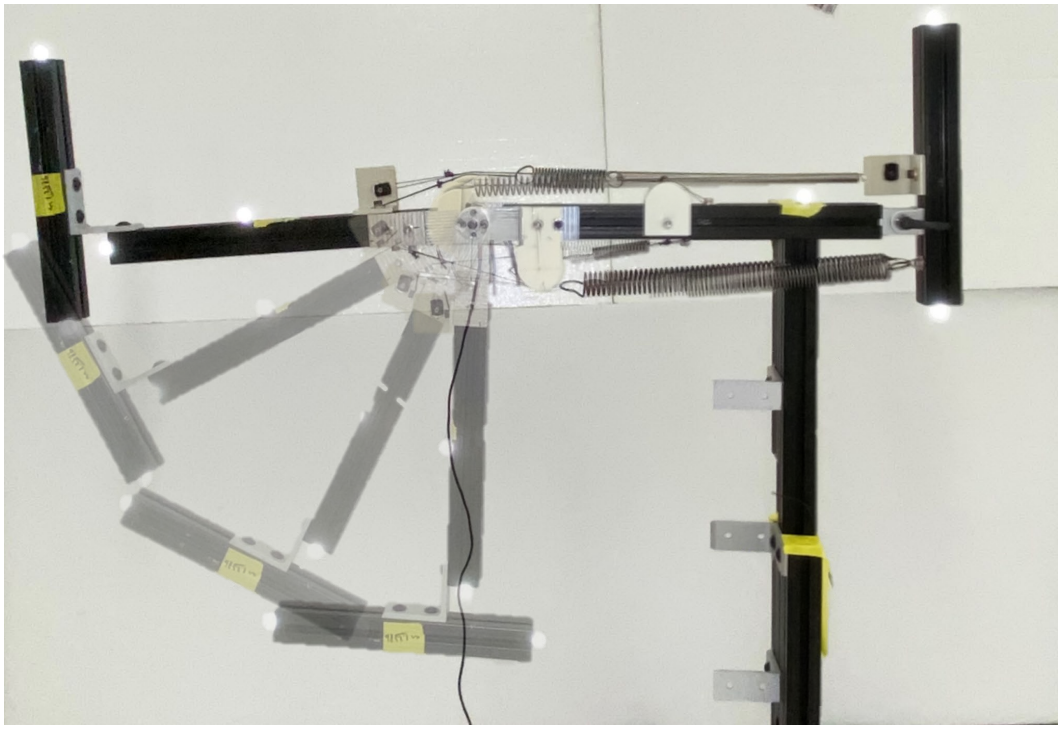

Figure 3.7: Replica leg experimental setup: Isokinetic knee flexion at hip 90

the model. To calculate the motion integration on multi-body dynamics was used.

$$\ddot{q} = [M(q)]^{-1}\{\tau_m + C(q,\dot{q}) + G(q) + F\} \tag{3.9}$$

Where $\ddot{q}$ is the coordinate accelerations created by joint torques(τ) , coriolis and centrifugal forces ($C\left(q,\dot{q}\right)$), gravity($G\left(q\right)$), and external forces applied to the model (F). q and $\dot{q}$ are coordinates and their velocities, and $[M(q)]^{-1}$ is the inverse of the mass matrix. The total torque net generated by muscles was calculated by following equation:

$$\tau_m = \left[R\left(q\right)\right] f\left(l_T, l_M\right) \tag{3.10}$$

The net moments, τ_m are a result of muscle moment arms, $R\left(q\right)$, multiplied by muscle passive forces, f, which is a function of muscle fiber lengths l_M and tendon lengthl_T. As forward dynamic calculates the states of the system $(\ddot{q}, \dot{q}, q)$ which includes the knee and ankle joint motion, velocities and acceleration. We used the output to compare with the reference motion and make an error curve.

Parameter Error Evaluation

Since the estimated values of ε_0 and ε_{T0} do not have a direct physiological representation of muscles, they need to be converted into musculotendon stiffness. The nonlinear behavior of musculotendon stiffness is illustrated by Equations 3.3 and 3.5, indicating that its value varies according to the muscle length changes. Nevertheless, to compare the estimated PMPs with previous studies, a single representative value is needed. Thus, we used the average stiffness of muscle-tendon at the initial length and the length at which maximum isometric force (F_M^0) occurs to introduce a constant number that represents musculotendon stiffness. The derivative of the equation 3.5 related to tendon length gives us the tendon stiffness:

$$\bar{K_T} = \frac{d\bar{F}_T}{d\bar{L}_T} = m_{kt} c_1 e^{\left(m_{kt} \cdot \left(\bar{L}_T - c_2\right)\right)} \tag{3.11}$$

Normalized stiffness at tendon slack length and the fiber strain at the maximum isometric force is:

$$\bar{K_T} = \begin{cases} m_{kt} & if \;\; \bar{L} = 1 \\ m_{kt}(1.2) & if \; \bar{L} = 1 + \varepsilon_0 \end{cases} \tag{3.12}$$

Taking average of both condition and considering the maximum isometric force F_M^0 and L_T^s the actual tendon stiffness is:

$$K_T = (\frac{F_M^0}{L_T^s})\ 1.1\ m_{kt} = \frac{1.97\ F_M^0}{\varepsilon_0\ L_T^s} \tag{3.13}$$

Alternatively, we can take the same approach to determine the muscle stiffness by differentiating equation 2 and obtaining the normalized muscle stiffness, as explained below. stiffness is:

$$\bar{K}_P = \frac{d\bar{F}^{PE}}{d\bar{L}_M} = \frac{k^{PE}}{\varepsilon_0} \cdot \frac{e^{\left(k^{PE}\left(\frac{\bar{L}_M - 1}{\varepsilon_0}\right)\right)} - b}{e^{k^{PE}} - b} = \frac{k^{PE}}{\varepsilon_0}\ \bar{F} \tag{3.14}$$

$$\bar{K}_P = \begin{cases} 0 & if\ \ \bar{L}_M = L_{min} \\ \frac{k^{PE}}{\varepsilon_0} & if\ \bar{L}_M = 1 + \varepsilon_0 \end{cases} \tag{3.15}$$

Similar to 3.13 The actual average stiffness considering F_M^0, L^T and k^{PE}=4 is [59]:

$$K_{P_{avg}} = \bar{K}_{P_{avg}} . \frac{F_M^0}{L_M^0} = \frac{2}{\varepsilon_0} \cdot \frac{F_M^0}{L_M^0} \tag{3.16}$$

And finally, parameter error is calculated by:

$$Error = \frac{P_e - P_r}{P_r} * 100(16) \tag{3.17}$$

Where P_e and P_r are optimal and reference parameters. Also, we reported the ε_0 and ε_{T_0} for extra details which can be helpful for future studies

Results

simulation

Figure 3.8 shows the results of the estimation error of optimal values for tendon slack length (TSL) in the fully-simulated method for various hip and ankle conditions. The estimation error for the main knee flexors/extensors is less than -0.032 %, except for calf muscles (gaslat, gasmed, soleus), which have an error of around -3.2 %. It is noteworthy that the TSL error of knee extensors decreases as the hip angle decreases from 90° to 15°, while the flexors muscles exhibit the lower error when the hip angle is 90°, causing them to be fully stretched. For example, the error of the semitendinosus muscle decreased from -3.2 % to -1 % when the knee changes from 90 to 0°. The error for calf muscles is also lower when the knee is at 0°. For instance, the error of the Soleus muscle decreased from -3.1 % at a knee angle of 90° to -1 % when the knee is at 0°. The negative error for most muscles suggests that the estimated TSL is less than the reference value in the musculoskeletal model. The results of the muscle stiffness error estimation are presented in Figure 3.9. The optimization procedure successfully estimated the muscle stiffness with an error of less than 3.5% across all conditions. The highest estimation error was observed for the rectus femoris muscle when the hip angle was 55°, while the error was close to zero at hip 15°. The semimembranosus muscle exhibited a noticeable change in error, decreasing from -1.5 % to 0.2 % and 0.05 % as the hip angle increased from 15 to 55 and 90° respectively. Similar to the TSL results, the error for flexor muscles was lower when the hip angle was 90°, whereas the error for extensor muscles decreased when the hip angle was 0°.

The maximum estimation error for the calf muscles was reported for the gastrocnemius medialis muscle, with a value of -0.1 %, while the estimation of the soleus muscle stiffness was nearly zero. The accuracy of muscle stiffness estimation for the calf muscles was highest when the knee

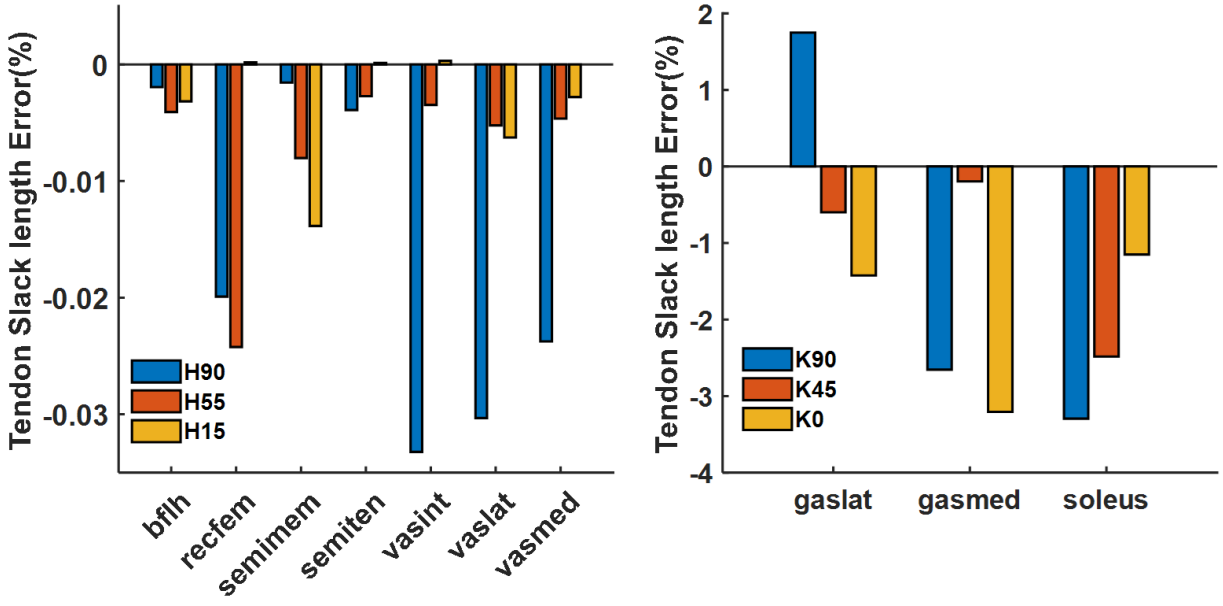

Figure 3.8: The estimation error for tendon slack length (TSL) varies among different muscles. The left chart illustrates TSL for knee flexor-extensors, excluding calf muscles, during knee flexion trials at hip angles of 90°, 55°, and 15° (blue, red, yellow). The right chart shows TSL for calf muscles during ankle plantar flexion trials at knee angles of 90°, 45°, and 0° (blue, red, yellow).

angle was 45°, with estimation errors of -0.01 %, -0.02 %, and nearly zero for the gastrocnemius lateralis, gastrocnemius medialis, and soleus muscles respectively.

The estimation error of Achilles tendon stiffness (TS) is presented in Figure 3.10. The maximum error of 63 % and -40 % is reported for the gastrocnemius lateral and gastrocnemius medial muscles, respectively, at a knee angle of 90°. However, this value was reduced to 4 % and 6 % when the knee angle was decreased to 0°. Similarly, the estimation error of TS for the Soleus muscle decreased from -25 % to 20 % and then 10 % as the knee angle decreased from 90 to 45 and 0° respectively.

The error between the reference data and the data generated from the forward dynamic applied on the model with optimized parameters in the ankle plantar flexion trial with different knee angles

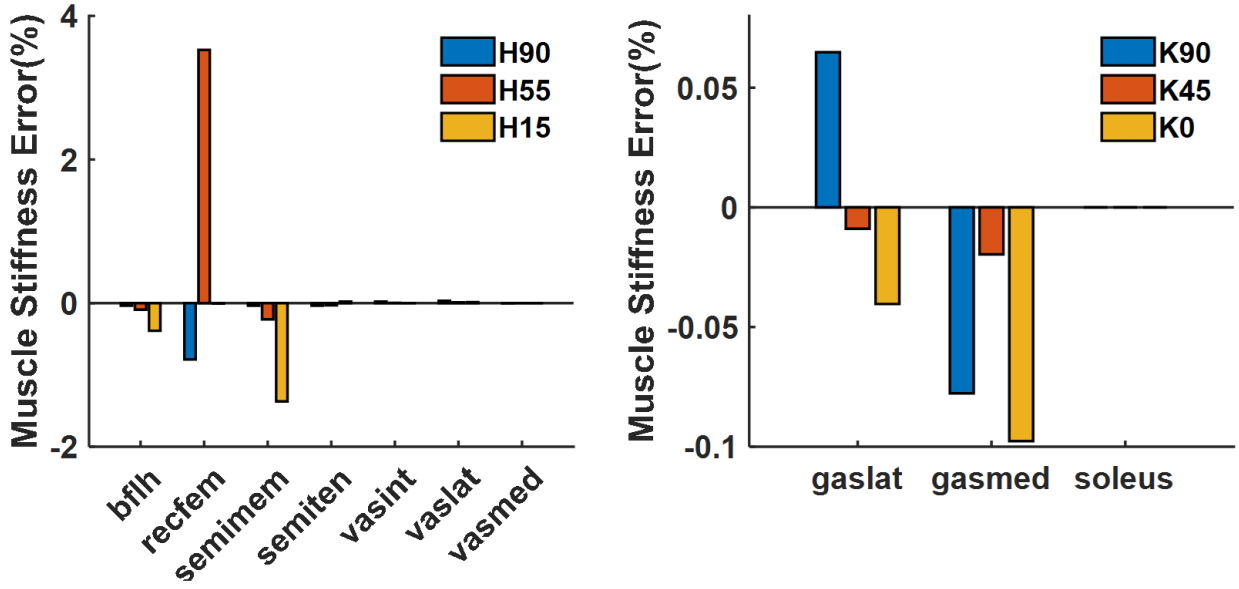

Figure 3.9: The estimation error of muscle stiffness among different muscles. The left chart illustrates muscle stiffness of knee flexor-extensors, excluding calf muscles, during knee flexion trials at hip angles of 90°, 55°, and 15° (blue, red, yellow). The right chart shows muscle stiffness of calf muscles during ankle plantar flexion trials at knee angles of 90°, 45°, and 0° (blue, red, yellow).

is shown in Figure3.11. The torque error remains consistently low, at around 0.05 $N.m$, for all sample times during ankle plantar flexion where the knee joint was setup at 45 and 0°. However, in the knee 90 trial, the error peaks at 0.35 $N.m$ at the beginning of the trial. Similarly, in terms of motion error, the knee 90 trial shows larger error of 0.1° at the beginning, while the error for the other trials remains less than 0.03°.

Replica leg

The experiment of knee flexion was conducted on Bio-inspired leg with hip 90° to determine the optimal resting position and stiffness for each spring. Figure 3.12 presents the calculated error between the optimal parameters and the actual stiffness of the springs. Among the springs,

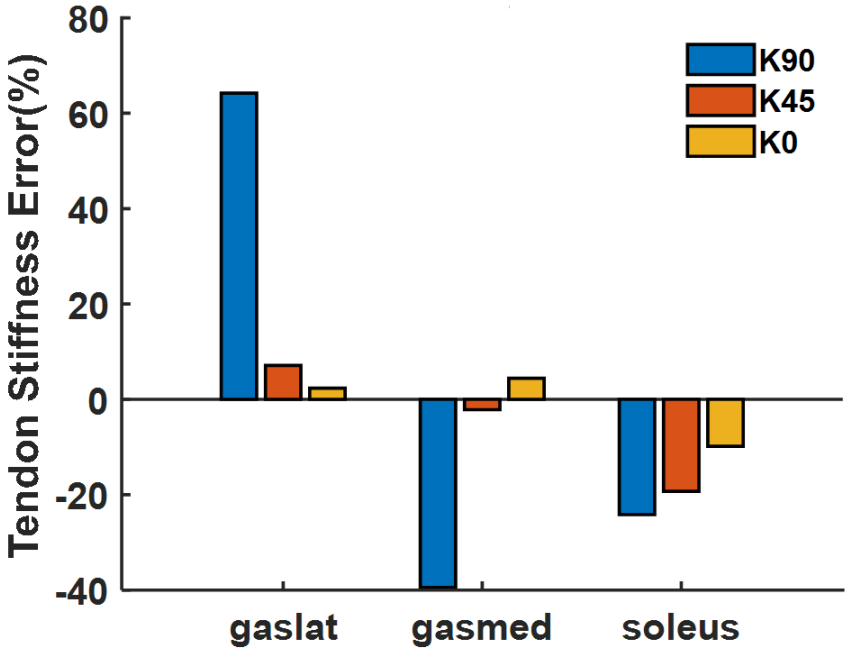

Figure 3.10: Tendon stiffness estimation error, for different knee angles of 90°, 45°, 0°

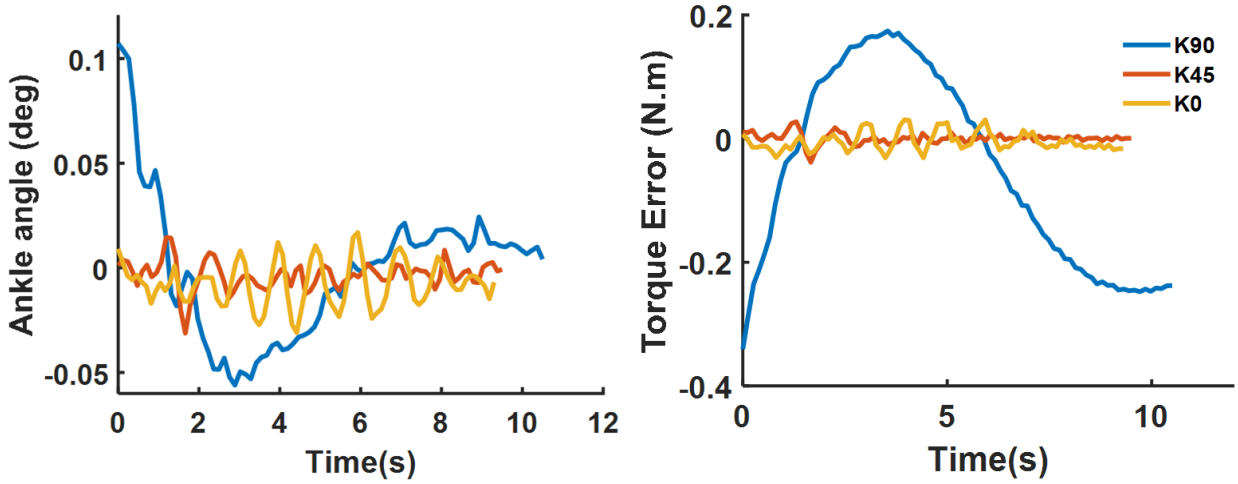

Figure 3.11: The error between the forward dynamic of optimized results and the reference motion.

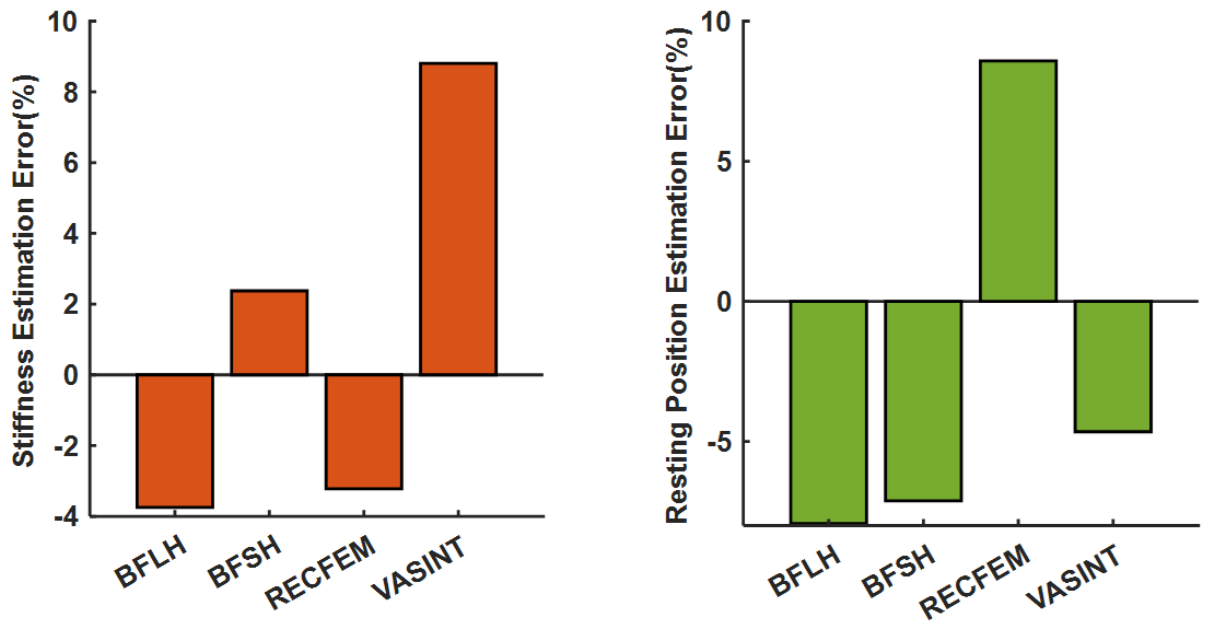

Figure 3.12: Optimized parameter including stiffness and resting position for all springs

VASINT exhibited the highest estimation error in stiffness, exceeding the actual value by 9 %. Conversely, BFLH and RECFEM showed estimation errors 3.9 % and 3.2 % lower than their respective actual stiffness values. The lowest error was observed in BFSH with a deviation of 2.3 %. Regarding the optimized resting position, the results mostly indicated values lower than the actual positions, with errors of 7.9 %, 7.1 %, and 4.6 % for BFLH, BFSH, and VASINT, respectively. The maximum error of 8.5 % was observed in RCFEM. A forward dynamics analysis was conducted on a replica leg with the optimized parameters to determine its similarity to the reference motion and torque. The joint angle derived from forward dynamics using the estimated parameters precisely matched the reference knee motion data, and the torque output was aligned with the experimental data (See Figure3.13).

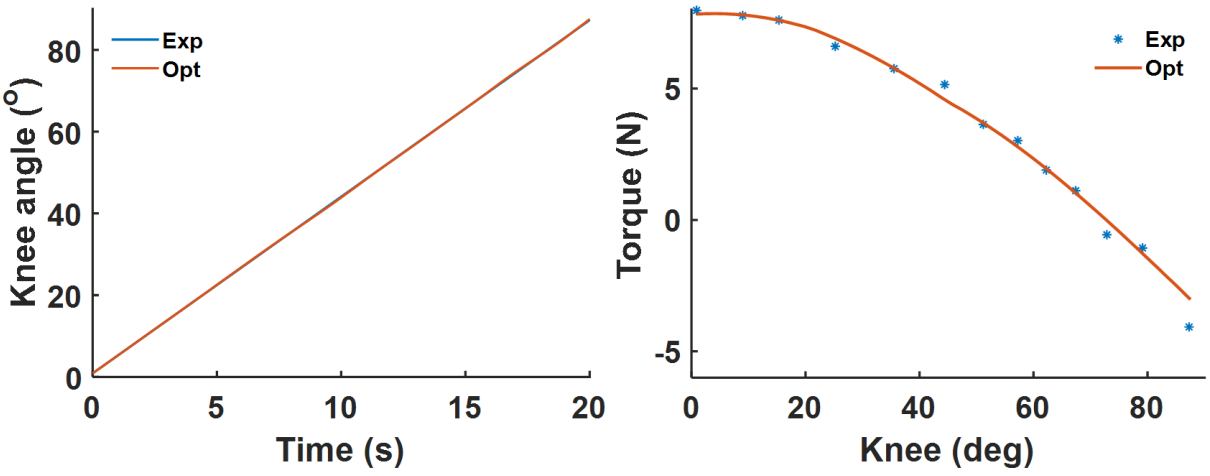

Figure 3.13: Optimized parameter including stiffness and resting position for all springs

In-vivo Method

Figure 3.14 illustrates a sample of torque measurements obtained using a dynamometer.The sample data corresponds to participant P9 and recorded during different low-speed knee flexion movements when the hip angle is set to 90°. The plot provides a visual representation of three distinct torque components. The blue line represents the total net torque, which encompasses the combined effects of the leg's weight and the passive muscle forces acting on the knee joint. The red line represents the torque generated specifically by the leg's weight and the passive muscle forces. The yellow line represents the torque resulting solely from the passive muscle forces. By isolating these factors, we can observe the contribution of the inherent passive force of the muscles to the overall torque profile.

A distinct trend can be observed in the torque generated by the passive forces as the knee undergoes a range of motion. Specifically, there is a sharp drop in torque from 0 to 20° of knee flexion, followed by a gradual decrease until the knee reaches 45°. Beyond this point, the torque continues

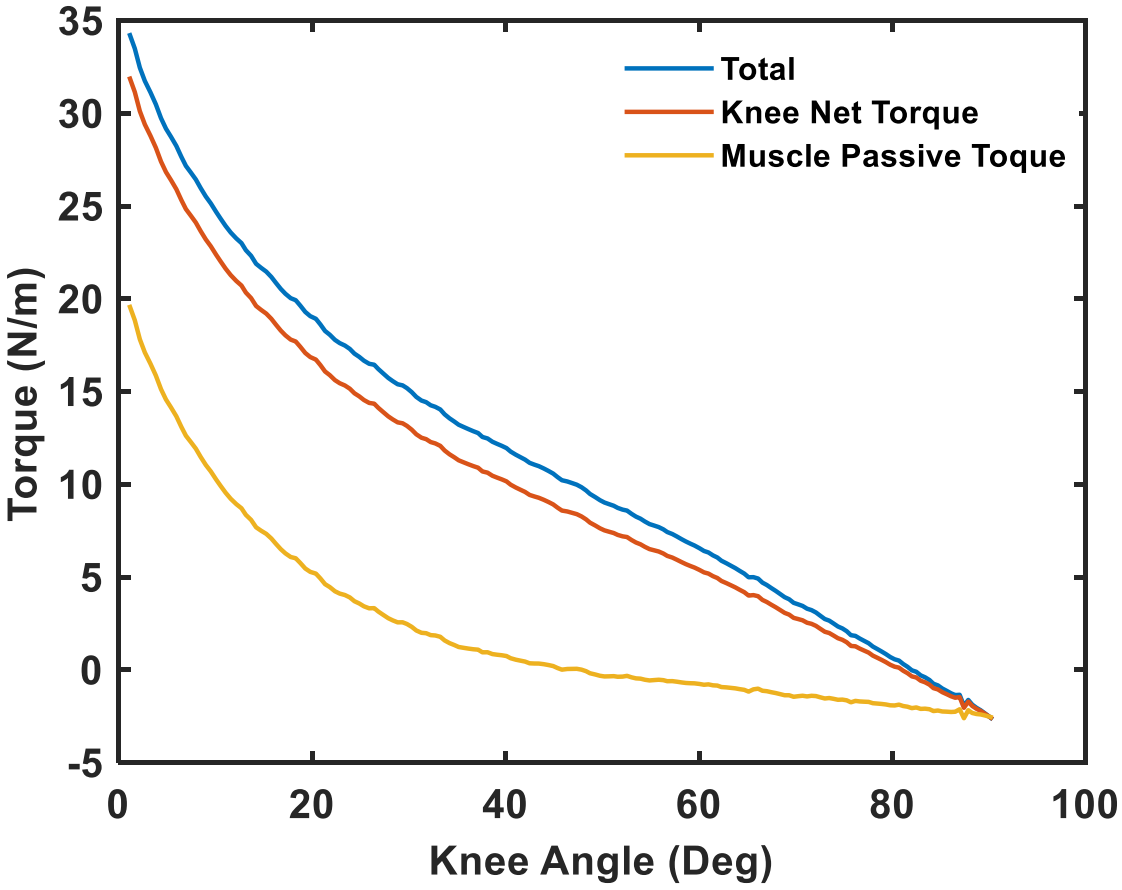

Figure 3.14: Torque analysis of experimental data during low speed isokinetic Knee Flexion Movements. Total net torque (blue line), the torque from the leg's weight and the passive muscle forces (red line), and the pure torque from the passive muscle forces only (yellow line)

to decrease in a linear fashion until it eventually reaches 0 at a knee angle of 90°.

Figure 3.15 presents the optimized tendon slack length (TSL) values from *in-vivo* method for different muscles among all participants and a generic model. The TSL values for the calf muscles (gaslat, gasmed) are normalized by the length of the shank (from the knee joint to the ankle joint), while the TSL values for the other muscles are normalized by the length of the thigh (from the hip joint to the knee joint). The bar chart displays the data, with each bar representing a specific

muscle. The blue box represents the Interquartile Range (IQR), and the blue line represents the median value.

For the calf muscles, the normalized TSL values are 0.95 [0.06] for gaslat, 0.96 [0.07] for gasmed, and 0.69 for soleus. The soleus muscle has the smallest IQR of [0.003] among all the muscles, indicating less variability in the TSL values. Among the other muscles, the highest normalized TSL is observed for semiten with a value of 1.13 [0.18]. This is followed by bflh with 1.116 [0.182], and refcfem with 1.1 [0.114]. Among the quadriceps muscles, Vasint has the highest normalized TSL of 0.7 and the lowest IQR of [0.025], while Vaslat and Vasmed have normalized TSL values of 0.65 [0.13] and 0.59 [0.18] respectively.

In addition to the optimized tendon slack length (TSL) values, we included the normalized TSL values of the generic Rajagopal model in the plot. To ensure a fair comparison, we replaced all the Millard muscles in the Rajagopal model with the Degroote model. The comparison between the optimized TSL values and the generic model revealed significant differences.

Specifically, for semiten, soleus, and vasint muscles, the TSL values of the generic model fell outside the Interquartile Range (IQR). The TSL value for semiten in the generic model was 0.68, which is 39 % less than the median value. For soleus, the generic model exhibited a TSL value of 0.75, which is 8 % higher than the median value. Additionally, the TSL value for vasint in the generic model was 0.56, which is 20 % less than the median value. Furthermore, the gaslat and gasmed exhibited TSL values on the upper fence, with gaslat at 1.02 and gasmed at 1.08. Figure 3.16 presents the calculated stiffness of the Achilles tendon, derived by summing the individual tendon stiffness values of the gaslat, gasmed, and soleus muscles. The optimized tendon parameter is reported as 421 [92] KN/m, indicating a higher stiffness compared to the generic model's tendon stiffness of 303 KN/m.

The knee flexor and extensor muscles with short tendons were considered as rigid, focusing solely

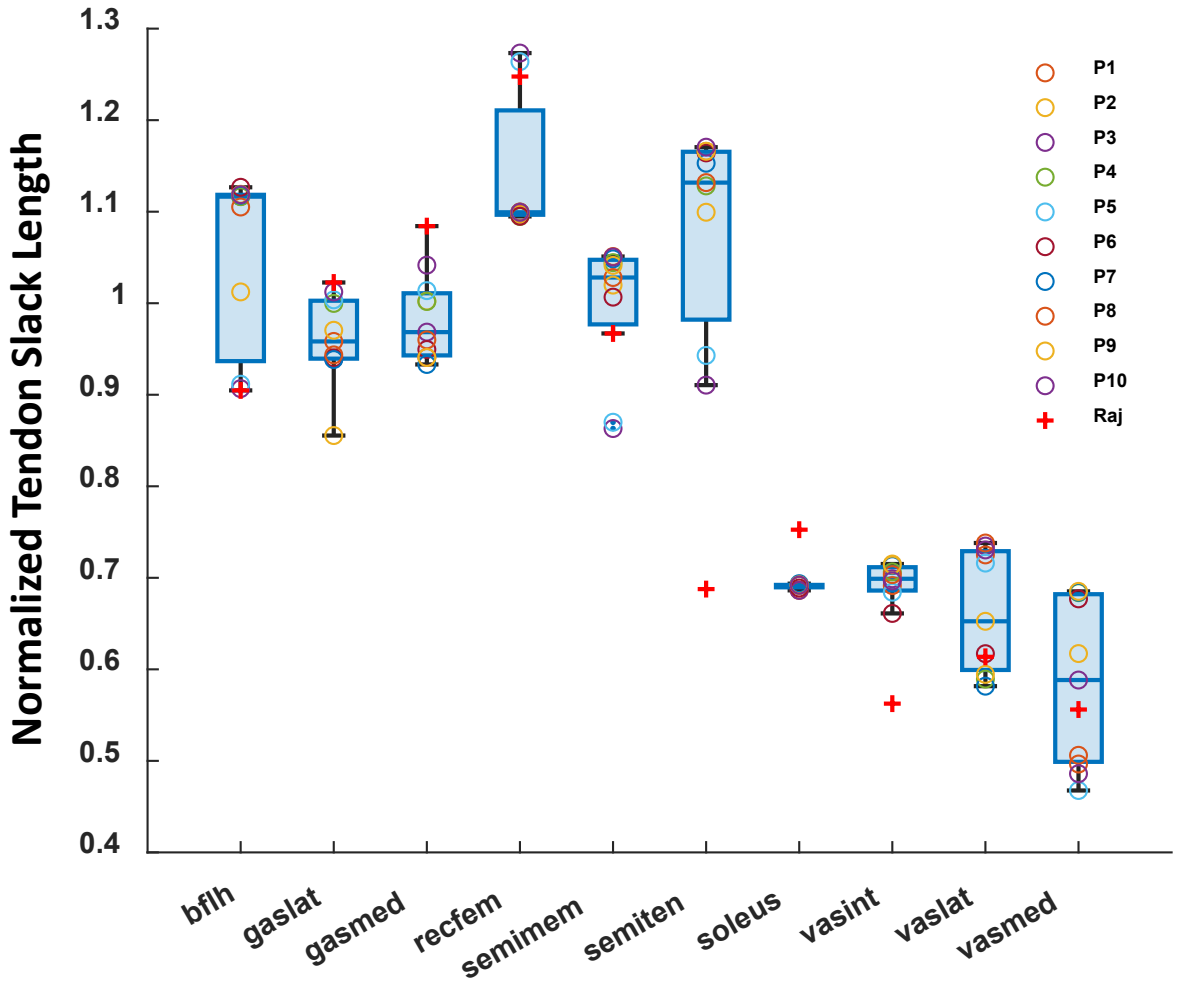

Figure 3.15: Normalized tendon slack length between participant. The central line within the box indicates the median value (blue line), while the box represents the interquartile range (IQR). the Data out of the bar are outliers

on optimizing their muscle stiffness for each individual participant. The optimized epsilon values obtained from the optimization process were then utilized in equation 14 to calculate the muscle stiffness when both the hip and knee angles were zero°. The results of the optimization of muscle stiffness for each individual are presented in Figure 3.17.

Among the knee flexor muscles, semimem demonstrated the highest stiffness with a value of 1.2

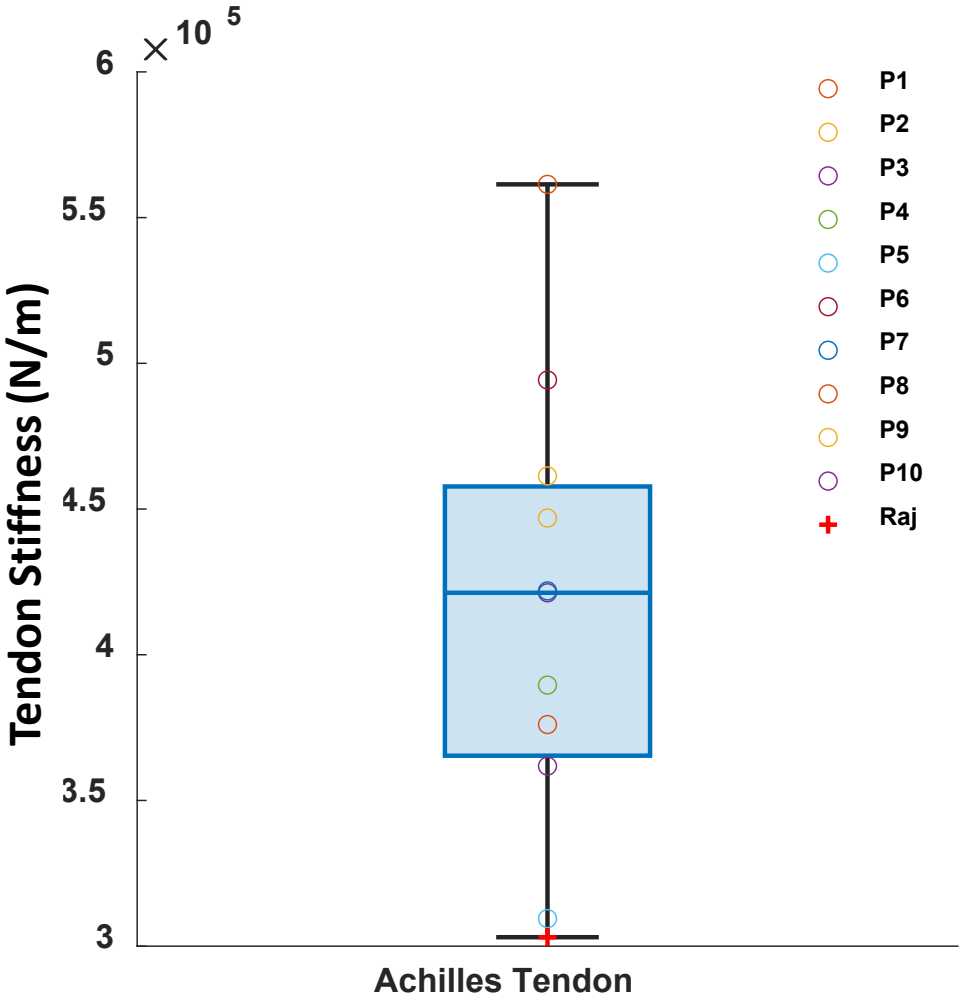

Figure 3.16: Inter-Participant Variability in Optimized Achilles Tendon Stiffness using the *In-Vivo Method*

[0.3] KN/m. Following semimem, bflh and semiten exhibited stiffness values of 802 [147] N/m and 473 [111] N/m respectively. The stiffness values of the quadriceps muscles, namely vasmed, vaslat, and vasint, were relatively close to each other, with approximate values of 936.8 [296] N/m, 861 [489] N/m, and 745 [246] N/m respectively, in descending order. Notably, recfem displayed the largest interquartile range (IQR) among the muscles, with a value of 922 [566], indicating

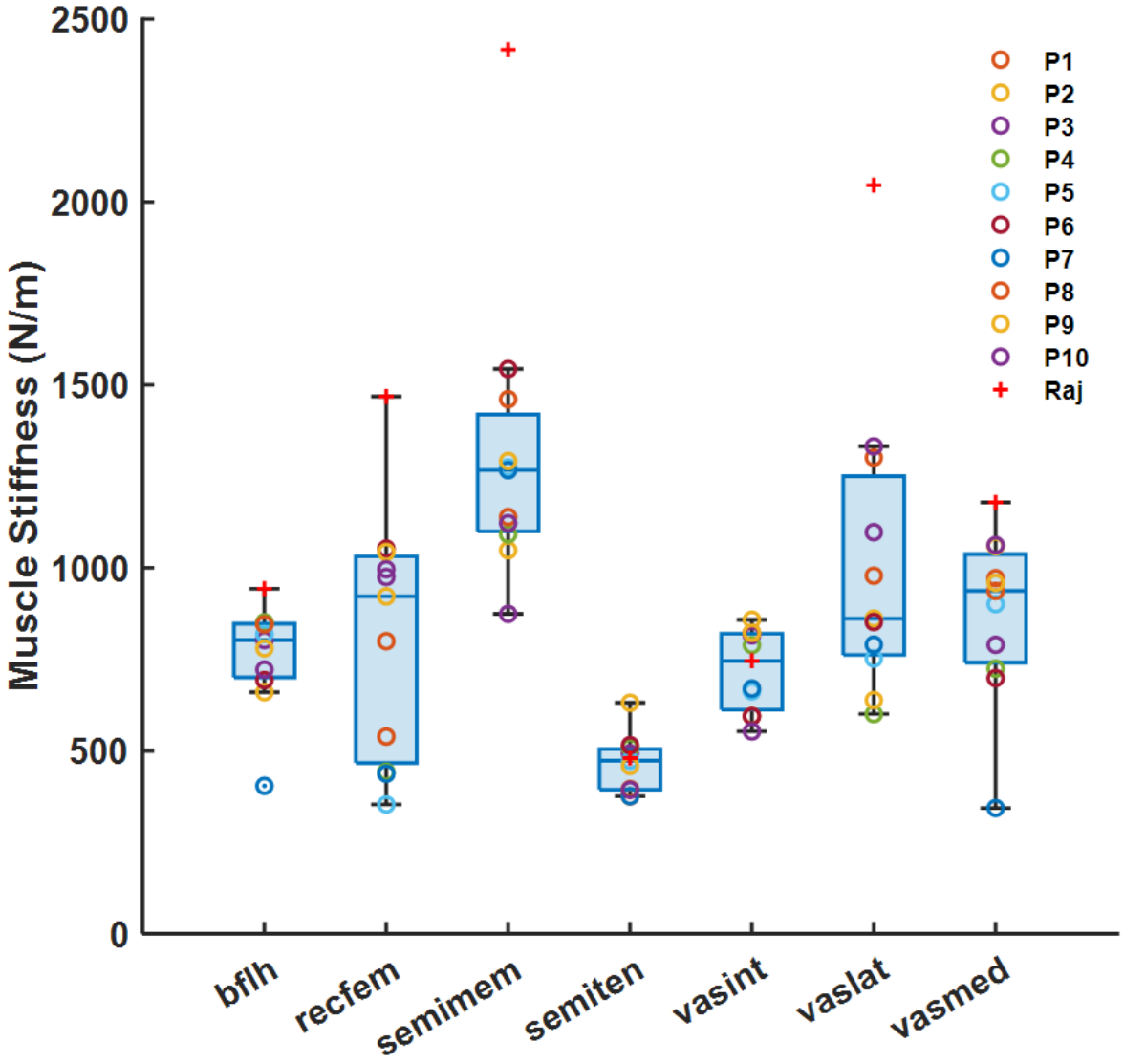

Figure 3.17: Optimization results of muscle stiffness for individual participants.

greater variability in stiffness compared to the other muscles. The muscle stiffness values obtained from the generic model were found to be significantly larger compared to the optimized values. Specifically, the generic stiffness value for semimem was 2.41 KN/m, which was 90 % higher than the corresponding optimized value. Similarly, the generic stiffness for vaslat was 2 KN/m, indicating an increase of 137 % compared to the optimized parameter.

Table 3.3: RMSE comparison between experimental and forward dynamics data for motion and torque across all participants in knee and ankle trials.

	RSME of Motion (°)		RSME of Torque ($N.m/kg$)	
	Ankle trial	Knee Trail	Ankle trial	Knee Trail
P1	0.009	0.058	0.0073	0.0093
P2	0.023	0.021	0.0275	0.0009
P3	0.792	1.648	0.0053	0.0256
P4	0.020	0.087	0.0079	0.0039
P5	0.007	0.205	0.0024	0.0209
P6	0.007	0.017	0.0035	0.0010
P7	0.040	0.267	0.0104	0.0122
P8	0.010	0.058	0.0147	0.0045
P9	0.026	0.095	0.0154	0.0067
P10	0.010	0.228	0.0149	0.0370
Avg	0.095	0.268	0.0109	0.0122

The optimized parameters obtained from experimental data were implemented in the model, and a comparison between the forward dynamic simulation and experimental data is presented in Table 3. The root mean square error (RMSE) was calculated to assess the agreement between the torque-time curve and motion-time curve of the experimental data and the forward dynamic simulation. The torque RMSE was normalized by the participants' body weight, while the knee angle, having the same range of motion for all participants, did not require normalization.

In the ankle trial, participant P3 exhibited the highest maximum error in motion, with 0.79°, while in the knee trial, the maximum error was 1.6° for the same subject. In most cases, the error for both ankle and knee trials was below 0.04 and 0.26°, respectively.The lowest RMSE values for the knee trial were achieved by P2 (0.87 $mN.m/Kg$), while for the ankle trial, the lowest RMSE value was obtained by P5 (2.4 $mN.m/Kg$). On the other hand, the highest RMSE value for the ankle trial was observed in P3 (27.5 $mN.m/Kg$), and for the knee trial, P10 had the highest RMSE value (37 $mN.m/Kg$). In the ankle trials the average RMSE of motion and torque among the all participants was 0.094° and 11 $mN.m/Kg$ while in knee trials these values were 0.56° and 12 $mN.m/Kg$.

Discussion

The results obtained from the three different methods provide valuable insights into the estimation of PMP and torque measurements. These findings shed light on the performance of the optimization algorithm and the accuracy of the musculotendon model in various experimental settings.

The result of fully simulated method indicated that the optimization procedure was successful in estimating the TSL and MS for most muscles, as the estimation errors remained below 3.5 % for TSL and MS Estimation across all conditions. Furthermore, we observed that the MS and TSL error for knee extensor muscles decreased as the hip angle decreased, while the flexor muscles exhibited lower error when the hip angle was 90°. Similarly, the TS estimation error of calf muscles decreased as the knee angle decreased to 0°. This suggests that the optimization error is reduced for muscles that are in a stretched position, as they have a higher contribution to generating net torque. These findings provide valuable insights for designing different motions for joints to increase the accuracy of optimization. Consistent with a previous study by [55], incorporating various motion patterns, including walking and squat jumping, which involve larger muscle stretches, has the potential to improve tendon slack length (TSL) optimization.

In simulation method the torque and motion errors were found to be correlated with errors in estimating the optimal parameters. In general a higher error in estimating the PMP resulted in larger errors in torque and motion. Building on this observation, a strategy was employed to select the best optimized parameters for each participant by utilizing a cost function that incorporated both motion and torque errors. The optimized parameter set with the lowest cost function value among all trials was identified and chosen as the optimal solution for that participant.

The successful validation of the optimization algorithm in estimating the parameters of replica leg that closely resembles the human leg demonstrates its reliability in determining human muscle

parameters. It is important to note that the replica leg was only run in the Hip90 condition. In this specific condition, the BFLH muscle was under tension at a knee angle of 0, and during knee flexion, the VASINT muscle was under tension. However, if the hip angle was set to 45 or 0, due to geometric restrictions of the mechanism and the limitations of the commercial spring, the BFLH muscle would not be adequately tensioned, resulting in a reduced contribution to the net torque. The available length of the desired stiffness was long and closely matched the distance between the wrapping object and the insertion point, leaving limited space for stretching the BFLH muscle. Also, differences in actuator type and joint structure between the robotic leg and the actual human leg may introduce errors in human experiments. For example, the linear spring used in the robotic leg experiment is a simplification of the nonlinear elastic component of passive human muscles. Additionally, the number of springs used in the leg experiment is fewer than the knee flexors and extensors in the human leg, resulting in fewer unknown parameters for optimization and a less complex task. Furthermore, the human knee is more complex than the simple hinge joint used in the robotic leg. Despite these simplifications, the leg replica was able to validate the performance and feasibility of estimating muscle stiffness and musculotendon slack length using optimization and experiment settings.

Achilles tendon plays in important role in energy efficient walking by utilizing energy recycling mechanism. As stiffness information can be used to calculate the level of energy storage and return [89], In the *in-vivo* we chose to estimate tendon stiffness rather than muscle. Also, this decision was made due to the convergence issues encountered when attempting to optimize both muscle and tendon stiffness simultaneously. The reason for this convergence problem can be attributed to the available experimental data. The experimental data only provided information on the total displacement and total force, without direct measurements of the displacement at the muscle-tendon junction. Consequently, the determination of stiffness values became an underdetermined problem, with an infinite number of potential solutions that could satisfy the given total

force and displacement. To address this challenge and facilitate the optimization process, the muscle stiffness values were utilized from the generic model for the calf muscles. This allowed for a focused optimization of the tendon stiffness, simplifying the problem and promoting convergence of the optimization algorithm. This limitation can be address by informing each muscle and tendon length using experimental method [25].

The observation from figure 3.14 suggests that the crucial phase for torque analysis lies within the range of 0 to 20° of knee flexion. The sharp drop in torque during this phase can be attributed to the full extension of all knee flexor muscles, resulting in the maximum stretch and the generation of substantial passive forces. Consequently, the data obtained during the early stages of knee flexion provides rich and informative input for the estimation of PMP.

The median of the optimized tendon slack length (TSL) values for the calf muscles was found to be lower compared to the values obtained from the generic model. Conversely, for other muscles, the median of the optimized TSL values was higher. These findings indicate that the average Achilles tendon length in the subject-specific model is shorter than that in the generic model. This aligns with the findings of Falisse [55], who also reported a decrease in TSL compared to the generic model.

Also, the optimized TSL values for the knee flexor and quadricep muscles were higher than those of the generic model while the optimized MS were lower than those of the Rajagopal model. These results suggest that the passive force generated by these muscles in the generic model is greater than the subject-specific model. Specifically, the optimized stiffness for the semimem and vaslat muscles were found to be 90 % and 137 % lower than the generic model, and their tendon slack lengthw were higher, leading to a drastic reduction in the passive force generated by these muscles.

In contrast, the estimated the level of semiten and vasint muscle stiffness aligned with the generic model. However, the etimated TSL for these muscles was considerably higher, leading to a reduc-

tion in muscle fiber length and, consequently, a decrease in the passive force generated by these muscles.

The Achilles tendon estimation results showed a 38 % increase compared to the generic model. Notably, this value is relatively closer, with only an 8 % difference, to the findings reported in a previous study by Muraoka [87], where a value of 390 (48) KN/m was reported. These findings emphasize the importance of making substantial adjustments to the parameters of the Degroote model in order to improve the accuracy of musculoskeletal modeling.

The limitation of our study is that we only utilized the results from one trial out of the nine conducted (three different joint conditions repeated three times) to determine the optimized parameters. However, for future studies, implementing a multi-phase optimization approach, where all trials are included, could provide a more comprehensive estimation by exposing the muscles to a wider range of stretched situations. This would likely lead to improved parameter estimation across all trials. Another limitation in our study is the assumption that the Achilles tendon is a summation of the individual tendon stiffness values of the calf muscles. To achieve a more accurate estimation, future improvements could involve refining the tendon model and considering a shared tendon for all three calf muscles. This approach may provide a closer estimation of the Achilles tendon properties and contribute to a more realistic representation of the musculoskeletal system.

Individuals with movement disorders, including stroke survivors [90,91] and children with cerebral palsy [92], often exhibit altered muscle characteristics. The estimation of PMPs can play a crucial role in modeling the walking patterns of individuals with movement disabilities [93,94].The implications of our study can be extended to evaluate PMPs in these specific populations and enhance the effectiveness of treatment methods [95–97].

Conclusion

In the first study we employed an optimization algorithm to develop a an easy-to-use, quantitative method of determining AFO stiffness. Estimated AFO stiffness were compared within the operators' trials and with theoretically calculated AFO stiffness to evaluate the accuracy of AADS tests. The AADS test results were repeatable through multiple trials and across operators. In low stiffness conditions, the AADS test had greater stiffness than actual results due to the friction of the AFO joint. As the spring strength increased, the AFO stiffness measured by AADS test was lower compared with actual stiffness due to the deformation of test AFO shells. The overall percent error between the theoretical and experimental stiffness was within ± 6%. Moreover, the AADS test had high precision among the different operators and trials. The quantitative measure of AFO stiffness will allow for tracking patient AFO prescription as the patient's optimal AFO stiffness changes as their situation progresses. It can help orthotists prescribe and fabricate new AFOs for their patient. In addition, a record of the AFO stiffness will also be beneficial in refabrication when the AFO is damaged or requires resizing as the patient grows.

In second study, We introduce a new method that enables comprehensive and accurate passive musculotendon parameters estimations using an optimal control optimization. Through a simulation-based analysis We observed that the prediction of muscle stiffness and tendon slack length had an error of less than 3.5%, while the error in tendon stiffness was less than 6% at a knee angle of zero. Secondly, using a simplified model of the human leg, we achieved a maximum estimation error of 9% for VASINT stiffness and an 8.5% error in resting position for RECTFEM. We assessed the accuracy of the proposed approach by comparing experimental data with data generated from forward dynamic simulations applied to subject-specific models with optimized parameters. The average root mean square error between experimental data and simulation output was less than 0.56° for joint angle, and it was less than 12mN.m/Kg for torque.

The method can help to evaluate the efficacy of the surgery methods and suggests refinements to the treatment based on desired stiffness. It can also be used to evaluate the outcomes of other treatments like stretch rehabilitation. Additionally, this method provides subject-specific muscle-tendon passive parameters for musculoskeletal analysis of children with cerebral palsy or athletic.

APPENDIX : COPYRIGHT PERMISSION

Creative Commons License Deed

Attribution 4.0 International (CC BY 4.0)

This is a human-readable summary of (and not a substitute for) the license.

You are free to:

Share — copy and redistribute the material in any medium or format

Adapt — remix, transform, and build upon the material

for any purpose, even commercially.

The licensor cannot revoke these freedoms as long as you follow the license terms.

Under the following terms:

Attribution — You must give appropriate credit, provide a link to the license, and indicate if changes were made. You may do so in any reasonable manner, but not in any way that suggests the licensor endorses you or your use.

No additional restrictions — You may not apply legal terms or technological measures that legally restrict others from doing anything the license permits.

Notices:

You do not have to comply with the license for elements of the material in the public domain or where your use is permitted by an applicable exception or limitation.

No warranties are given. The license may not give you all of the permissions necessary for your intended use. For example, other rights such as publicity, privacy, or moral rights may limit how you use the material.

LIST OF REFERENCES

[1] M. Millard, T. Uchida, A. Seth, and S. L. Delp, "Flexing computational muscle: Modeling and simulation of musculotendon dynamics," *Journal of Biomechanical Engineering*, vol. 135, no. 2, 2013.

[2] F. Topputo and C. Zhang, "Survey of direct transcription for low-thrust space trajectory optimization with applications," *Abstract and Applied Analysis*, vol. 2014, p. 851720, 2014.

[3] P. M. Kluding, K. Dunning, M. W. O'Dell, S. S. Wu, J. Ginosian, J. Feld, and K. McBride, "Foot drop stimulation versus ankle foot orthosis after stroke: 30-week outcomes," *Stroke*, vol. 44, no. 6, pp. 1660–9, 2013.

[4] N. B. Bolus, C. N. Teague, O. T. Inan, and G. F. Kogler, "Instrumented ankle–foot orthosis: Toward a clinical assessment tool for patient-specific optimization of orthotic ankle stiffness," *IEEE/ASME Transactions on Mechatronics*, vol. 22, no. 6, pp. 2492–2501, 2017.

[5] D. Totah, M. Menon, C. Jones-Hershinow, K. Barton, and D. H. Gates, "The impact of ankle-foot orthosis stiffness on gait: A systematic literature review," *Gait & Posture*, vol. 69, pp. 101–111, 2019.

[6] T. M. Winters, M. Takahashi, R. L. Lieber, and S. R. Ward, "Whole muscle length-tension relationships are accurately modeled as scaled sarcomeres in rabbit hindlimb muscles," *Journal of Biomechanics*, vol. 44, no. 1, pp. 109–115, 2011.

[7] C. N. Maganaris and J. P. Paul, "Tensile properties of the in vivo human gastrocnemius tendon," *Journal of Biomechanics*, vol. 35, no. 12, pp. 1639–1646, 2002.

[8] P. Gerus, G. Rao, and E. Berton, "Subject-specific tendon-aponeurosis definition in hill-type model predicts higher muscle forces in dynamic tasks," *PLOS ONE*, vol. 7, no. 8, pp. 1–13, 08 2012.

[9] J. F. Carlsen, M. R. Pedersen, C. Ewertsen, A. Săftoiu, L. Lönn, S. R. Rafaelsen, and M. B. Nielsen, "A comparative study of strain and shear-wave elastography in an elasticity phantom," *American Journal of Roentgenology*, vol. 204, no. 3, pp. W236–W242, 2015.

[10] L. Chernak, R. DeWall, K. Lee, and D. Thelen, "Length and activation dependent variations in muscle shear wave speed," *Physiological measurement*, vol. 34, no. 6, p. 713, 2013.

[11] S. F. Eby, P. Song, S. Chen, Q. Chen, J. F. Greenleaf, and K.-N. An, "Validation of shear wave elastography in skeletal muscle," *Journal of biomechanics*, vol. 46, no. 14, pp. 2381–2387, 2013.

[12] J.-L. Gennisson, T. Deffieux, E. Macé, G. Montaldo, M. Fink, and M. Tanter, "Viscoelastic and anisotropic mechanical properties of in vivo muscle tissue assessed by supersonic shear imaging," *Ultrasound in medicine & biology*, vol. 36, no. 5, pp. 789–801, 2010.

[13] S. Ramezani, B. Brady, H. Kim, M. K. Carroll, and H. Choi, "A method for quantifying stiffness of ankle-foot orthoses through motion capture and optimization algorithm," *IEEE Access*, vol. 10, pp. 58 930–58 937, 2022.

[14] D. J. Bregman, M. M. van der Krogt, V. de Groot, J. Harlaar, M. Wisse, and S. H. Collins, "The effect of ankle foot orthosis stiffness on the energy cost of walking: a simulation study," *Clin Biomech (Bristol, Avon)*, vol. 26, no. 9, pp. 955–61, 2011.

[15] B. Chen, B. Zi, Y. Zeng, L. Qin, and W.-H. Liao, "Ankle-foot orthoses for rehabilitation and reducing metabolic cost of walking: Possibilities and challenges," *Mechatronics*, vol. 53, pp. 241–250, 2018.

[16] T. Sumiya, Y. Suzuki, and T. Kasahara, "Stiffness control in posterior-type plastic ankle-foot orthoses: effect of ankle trimline. part 2: Orthosis characteristics and orthosis/patient matching," *Prosthet Orthot Int*, vol. 20, no. 2, pp. 132–7, 1996.

[17] Y. L. Kerkum, A. I. Buizer, J. C. van den Noort, J. G. Becher, J. Harlaar, and M. A. Brehm, "The effects of varying ankle foot orthosis stiffness on gait in children with spastic cerebral palsy who walk with excessive knee flexion," *PLoS One*, vol. 10, no. 11, p. e0142878, 2015.

[18] N. F. J. Waterval, F. Nollet, J. Harlaar, and M.-A. Brehm, "Modifying ankle foot orthosis stiffness in patients with calf muscle weakness: gait responses on group and individual level," *Journal of NeuroEngineering and Rehabilitation*, vol. 16, no. 1, p. 120, 2019.

[19] S. Yamamoto, S. Miyazaki, and T. Kubota, "Quantification of the effect of the mechanical property of ankle-foot orthoses on hemiplegic gait," *Gait & Posture*, vol. 1, no. 1, pp. 27–34, 1993.

[20] K. Desloovere, G. Molenaers, L. Van Gestel, C. Huenaerts, A. Van Campenhout, B. Callewaert, P. Van de Walle, and J. Seyler, "How can push-off be preserved during use of an ankle foot orthosis in children with hemiplegia? a prospective controlled study," *Gait Posture*, vol. 24, no. 2, pp. 142–51, 2006.

[21] M. A. Brehm, J. Harlaar, and M. Schwartz, "Effect of ankle-foot orthoses on walking efficiency and gait in children with cerebral palsy," *J Rehabil Med*, vol. 40, no. 7, pp. 529–34, 2008.

[22] I. Skaaret, H. Steen, T. Terjesen, and I. Holm, "Impact of ankle-foot orthoses on gait 1 year after lower limb surgery in children with bilateral cerebral palsy," *Prosthet Orthot Int*, vol. 43, no. 1, pp. 12–20, 2019.

[23] N. S. Thompson, T. C. Taylor, K. R. McCarthy, A. P. Cosgrove, and R. J. Baker, "Effect of a rigid ankle-foot orthosis on hamstring length in children with hemiplegia," *Dev Med Child Neurol*, vol. 44, no. 1, pp. 51–7, 2002.

[24] H. Choi, K. M. Peters, M. B. MacConnell, K. K. Ly, E. S. Eckert, and K. M. Steele, "Impact of ankle foot orthosis stiffness on achilles tendon and gastrocnemius function during unimpaired gait," *Journal of Biomechanics*, vol. 64, pp. 145–152, 2017.

[25] H. Choi, T. A. L. Wren, and K. M. Steele, "Gastrocnemius operating length with ankle foot orthoses in cerebral palsy," *Prosthet Orthot Int*, vol. 41, no. 3, pp. 274–285, 2017.

[26] D. Adiputra, N. Nazmi, I. Bahiuddin, U. Ubaidillah, F. Imaduddin, M. A. Abdul Rahman, S. A. Mazlan, and H. Zamzuri, "A review on the control of the mechanical properties of ankle foot orthosis for gait assistance," *Actuators*, vol. 8, no. 1, p. 10, 2019.

[27] K. Kane, P. Manns, J. Lanovaz, and K. Musselman, "Clinician perspectives and experiences in the prescription of ankle-foot orthoses for children with cerebral palsy," *Physiotherapy Theory and Practice*, vol. 35, no. 2, pp. 148–156, 2019.

[28] E. Vasiliauskaite, A. Ielapi, M. De Beule, W. Van Paepegem, J. P. Deckers, M. Vermandel, M. Forward, and F. Plasschaert, "A study on the efficacy of afo stiffness prescriptions," *Disabil Rehabil Assist Technol*, vol. 16, no. 1, pp. 27–39, 2021.

[29] D. J. Bregman, A. Rozumalski, D. Koops, V. de Groot, M. Schwartz, and J. Harlaar, "A new method for evaluating ankle foot orthosis characteristics: Bruce," *Gait & Posture*, vol. 30, no. 2, pp. 144–9, 2009.

[30] B. R. Shuman and E. Russell Esposito, "Multiplanar stiffness of commercial carbon composite ankle-foot orthoses," *Journal of Biomechanical Engineering*, vol. 144, no. 1, pp. 1–8, 2021.

[31] A. Ielapi, E. Vasiliauskaite, M. Hendrickx, M. Forward, N. Lammens, W. Van Paepegem, J. P. Deckers, M. Vermandel, and M. De Beule, "A novel experimental setup for evaluating the stiffness of ankle foot orthoses," *BMC Research Notes*, vol. 11, no. 1, p. 649, 2018.

[32] T. Kobayashi, A. K. L. Leung, and S. W. Hutchins, "Techniques to measure rigidity of ankle-foot orthosis: A review," *Journal of Rehabilitation Research and Development*, vol. 48, no. 5, p. 565–576, 2011.

[33] P. Cappa, F. Patane', and M. M. Pierro, "A novel device to evaluate the stiffness of ankle-foot orthosis devices," *Journal of Biomechanical Engineering*, vol. 125, no. 6, pp. 913–917, 2004.

[34] P. Cappa, F. Patanè, and G. Di Rosa, "A continuous loading apparatus for measuring three-dimensional stiffness of ankle-foot orthoses," *Journal of Biomechanical Engineering*, vol. 127, no. 6, pp. 1025–1029, 2005.

[35] F. Gao, W. Carlton, and S. Kapp, "Development of a motorized device for quantitative investigation of articulated afo misalignment," in *2010 4th International Conference on Bioinformatics and Biomedical Engineering*, 2010, pp. 1–4.

[36] F. Gao., W. Carlton, and S. Kapp, "Effects of joint alignment and type on mechanical properties of thermoplastic articulated ankle foot orthosis," *Prosthetics and Orthotics International*, vol. 35, no. 2, pp. 181–189, 2011.

[37] K. R. Ashcraft and A. M. Grabowski, "Characterizing the mechanical stiffness of passive-dynamic ankle-foot orthosis struts," *Frontiers in Rehabilitation Sciences*, vol. 3, 2022.

[38] N. G. Harper, E. R. Esposito, J. M. Wilken, and R. R. Neptune, "The influence of ankle-foot orthosis stiffness on walking performance in individuals with lower-limb impairments," *Clin Biomech (Bristol, Avon)*, vol. 29, no. 8, pp. 877–84, 2014.

[39] M. Yamamoto, K. Shimatani, H. Okano, and H. Takemura, "Effect of ankle-foot orthosis stiffness on muscle force during gait through mechanical testing and gait simulation," *IEEE Access*, vol. 9, pp. 98 039–98 047, 2021.

[40] A. Wach, L. McGrady, M. Wang, and B. Silver-Thorn, "Assessment of mechanical characteristics of ankle-foot orthoses," *J Biomech Eng*, vol. 140, no. 7, pp. 1–6, 2018.

[41] M. P. Kadaba, H. K. Ramakrishnan, and M. E. Wootten, "Measurement of lower extremity kinematics during level walking," *Journal of Orthopaedic Research*, vol. 8, no. 3, pp. 383–392, 1990.

[42] S. L. Delp, F. C. Anderson, A. S. Arnold, P. Loan, A. Habib, C. T. John, E. Guendelman, and D. G. Thelen, "Opensim: open-source software to create and analyze dynamic simulations of movement," *IEEE Trans Biomed Eng*, vol. 54, no. 11, pp. 1940–50, 2007.

[43] U. Della Croce, A. Leardini, L. Chiari, and A. Cappozzo, "Human movement analysis using stereophotogrammetry: Part 4: assessment of anatomical landmark misplacement and its effects on joint kinematics," *Gait & Posture*, vol. 21, no. 2, pp. 226–237, 2005.

[44] W. Koller, A. Baca, and H. Kainz, "Impact of scaling errors of the thigh and shank segments on musculoskeletal simulation results," *Gait & Posture*, vol. 87, pp. 65–74, 2021.

[45] I. Symeonidis, G. Kavadarli, E. Schuller, and S. Peldschus, "Simulation of biomechanical experiments in opensim," in *XII Mediterranean Conference on Medical and Biological Engineering and Computing 2010*, P. D. Bamidis and N. Pallikarakis, Eds. Berlin, Heidelberg: Springer Berlin Heidelberg, 2010, pp. 107–110.

[46] L. Sthle and S. Wold, "Analysis of variance (anova)," *Chemometrics and Intelligent Laboratory Systems*, vol. 6, no. 4, pp. 259–272, 1989.

[47] K. J. Jem, J. F. van der Pol, and S. de Vos, *Microbial Lactic Acid, Its Polymer Poly(lactic acid), and Their Industrial Applications*. Berlin, Heidelberg: Springer Berlin Heidelberg, 2010, pp. 323–346.

[48] E. M. Arnold, S. R. Ward, R. L. Lieber, and S. L. Delp, "A model of the lower limb for analysis of human movement," *Annals of biomedical engineering*, vol. 38, no. 2, pp. 269–279, 2010.

[49] F. Schellenberg, W. R. Taylor, I. Jonkers, and S. Lorenzetti, "Robustness of kinematic weighting and scaling concepts for musculoskeletal simulation," *Computer methods in BiomeChaniCs and BiomediCal engineering*, vol. 20, no. 7, pp. 720–729, 2017.

[50] S. M. Morrison, T. J. Dick, and J. M. Wakeling, "Structural and mechanical properties of the human achilles tendon: Sex and strength effects," *Journal of Biomechanics*, vol. 48, no. 12, pp. 3530–3533, 2015.

[51] K. Kubo, "Active muscle stiffness in the human medial gastrocnemius muscle in vivo," *Journal of Applied Physiology*, vol. 117, no. 9, pp. 1020–1026, 2014, pMID: 25170073.

[52] M. Bernabei, S. S. Lee, E. J. Perreault, and T. G. Sandercock, "Shear wave velocity is sensitive to changes in muscle stiffness that occur independently from changes in force," *Journal of applied physiology*, vol. 128, no. 1, pp. 8–16, 2020.

[53] B. A. Garner and M. G. Pandy, "Estimation of musculotendon properties in the human upper limb," *Annals of Biomedical Engineering*, vol. 31, no. 2, pp. 207–220, 2003.

[54] M. A. King and M. R. Yeadon, "Determining subject-specific torque parameters for use in a torque-driven simulation model of dynamic jumping," *Journal of Applied Biomechanics*, vol. 18, no. 3, pp. 207 – 217, 2002.

[55] A. Falisse, S. Van Rossom, I. Jonkers, and F. De Groote, "Emg-driven optimal estimation of subject-specific hill model muscle–tendon parameters of the knee joint actuators," *IEEE Transactions on Biomedical Engineering*, vol. 64, no. 9, pp. 2253–2262, 2016.

[56] F. E. Zajac, "Muscle and tendon: properties, models, scaling, and application to biomechanics and motor control," *Critical reviews in biomedical engineering*, vol. 17, no. 4, pp. 359–411, 1989.

[57] A. V. Hill, "The heat of shortening and the dynamic constants of muscle," *Proceedings of the Royal Society of London. Series B-Biological Sciences*, vol. 126, no. 843, pp. 136–195, 1938.

[58] F. Heinen, S. N. Sørensen, M. King, M. Lewis, M. E. Lund, J. Rasmussen, and M. de Zee, "Muscle-tendon unit parameter estimation of a hill-type musculoskeletal model based on experimentally obtained subject-specific torque profiles," *Journal of biomechanical engineering*, vol. 141, no. 6, p. 061005, 2019.

[59] C. L. Dembia, N. A. Bianco, A. Falisse, J. L. Hicks, and S. L. Delp, "Opensim moco: Musculoskeletal optimal control," *bioRxiv*, p. 839381, 2019.

[60] G. Wanner and E. Hairer, *Solving Ordinary Differential Equations*. New York: Springer Berlin Heidelberg, 1996, vol. 375.

[61] Y.-C. Lin and M. G. Pandy, "Three-dimensional data-tracking dynamic optimization simulations of human locomotion generated by direct collocation," *Journal of biomechanics*, vol. 59, pp. 1–8, 2017.

[62] N. Mehrabi, M. H. Schwartz, and K. M. Steele, "Can altered muscle synergies control unimpaired gait?" *Journal of biomechanics*, vol. 90, pp. 84–91, 2019.

[63] M. Ackermann and A. J. Van den Bogert, "Optimality principles for model-based prediction of human gait," *Journal of biomechanics*, vol. 43, no. 6, pp. 1055–1060, 2010.

[64] J. K. Moore and A. J. van den Bogert, "opty: Software for trajectory optimization and parameter identification using direct collocation," *Journal of Open Source Software*, 2018.

[65] S. Porsa, Y.-C. Lin, and M. G. Pandy, "Direct methods for predicting movement biomechanics based upon optimal control theory with implementation in opensim," *Annals of biomedical engineering*, vol. 44, no. 8, pp. 2542–2557, 2016.

[66] F. De Groote, A. L. Kinney, A. V. Rao, and B. J. Fregly, "Evaluation of direct collocation optimal control problem formulations for solving the muscle redundancy problem," *Annals of biomedical engineering*, vol. 44, no. 10, pp. 2922–2936, 2016.

[67] F. Rohani, H. Richter, and A. J. Van den Bogert, "Optimal design and control of an electromechanical transfemoral prosthesis with energy regeneration," *PloS one*, vol. 12, no. 11, p. e0188266, 2017.

[68] A. Seth, J. L. Hicks, T. K. Uchida, A. Habib, C. L. Dembia, J. J. Dunne, C. F. Ong, M. S. DeMers, A. Rajagopal, M. Millard, S. R. Hamner, E. M. Arnold, J. R. Yong, S. K. Lakshmikanth, M. A. Sherman, J. P. Ku, and S. L. Delp, "Opensim: Simulating musculoskeletal dynamics and neuromuscular control to study human and animal movement," *PLOS Computational Biology*, vol. 14, no. 7, p. e1006223, 2018.

[69] A. Del Buono, O. Chan, and N. Maffulli, "Achilles tendon: functional anatomy and novel emerging models of imaging classification," *Int Orthop*, vol. 37, no. 4, pp. 715–21, 2013.

[70] A. Rajagopal, C. L. Dembia, M. S. DeMers, D. D. Delp, J. L. Hicks, and S. L. Delp, "Full-body musculoskeletal model for muscle-driven simulation of human gait," *IEEE transactions on biomedical engineering*, vol. 63, no. 10, pp. 2068–2079, 2016.

[71] S. K. Gollapudi and D. C. Lin, "Experimental determination of sarcomere force–length relationship in type-i human skeletal muscle fibers," *Journal of Biomechanics*, vol. 42, no. 13, pp. 2011–2016, 2009.

[72] S. P. Magnusson, P. Aagaard, S. Rosager, P. Dyhre-Poulsen, and M. Kjaer, "Load-displacement properties of the human triceps surae aponeurosis in vivo," *The Journal of physiology*, vol. 531, no. 1, pp. 277–288, 2001.

[73] D. G. Thelen, "Adjustment of muscle mechanics model parameters to simulate dynamic contractions in older adults," *Journal of Biomechanical Engineering*, vol. 125, no. 1, pp. 70–77, 2003.

[74] D. G. Thelen, F. C. Anderson, and S. L. Delp, "Generating dynamic simulations of movement using computed muscle control," *J Biomech*, vol. 36, no. 3, pp. 321–8, 2003.

[75] D. G. Lloyd and T. F. Besier, "An emg-driven musculoskeletal model to estimate muscle forces and knee joint moments in vivo," *J Biomech*, vol. 36, no. 6, pp. 765–76, 2003.

[76] D. J. Farris, J. L. Hicks, S. L. Delp, and G. S. Sawicki, "Musculoskeletal modelling deconstructs the paradoxical effects of elastic ankle exoskeletons on plantar-flexor mechanics and energetics during hopping," *J Exp Biol*, vol. 217, no. Pt 22, pp. 4018–28, 2014.

[77] R. W. Jackson, C. L. Dembia, S. L. Delp, and S. H. Collins, "Muscle-tendon mechanics explain unexpected effects of exoskeleton assistance on metabolic rate during walking," *J Exp Biol*, vol. 220, no. Pt 11, pp. 2082–2095, 2017.

[78] T. Geijtenbeek, "Scone: Open source software for predictive simulation of biological motion," *Journal of Open Source Software*, vol. 4, no. 38, p. 1421, 2019.

[79] F. O. Carmichael, G. Thomas, L. H. Jennifer, and L. D. Scott, "Predicting gait adaptations due to ankle plantarflexor muscle weakness and contracture using physics-based musculoskeletal simulations," *bioRxiv*, p. 597294, 2019.

[80] M. L. Handford and M. Srinivasan, "Robotic lower limb prosthesis design through simultaneous computer optimizations of human and prosthesis costs," *Scientific Reports*, vol. 6, no. 1, p. 19983, 2016.

[81] P. Puchaud, F. Bailly, and M. Begon, "Direct multiple shooting and direct collocation perform similarly in biomechanical predictive simulations," 2023.

[82] M. Diehl, H. Bock, H. Diedam, and P.-B. Wieber, *Fast Direct Multiple Shooting Algorithms for Optimal Robot Control*. Berlin, Heidelberg: Springer Berlin Heidelberg, 2006, pp. 65–93. [Online]. Available: https://doi.org/10.1007/978-3-540-36119-0_4

[83] J. T. Blackburn and D. N. Pamukoff, "Geometric and architectural contributions to hamstring musculotendinous stiffness," *Clinical Biomechanics*, vol. 29, no. 1, pp. 105–110, 2014.

[84] G. Le Sant, A. Nordez, R. Andrade, F. Hug, S. Freitas, and R. Gross, "Stiffness mapping of lower leg muscles during passive dorsiflexion," *Journal of anatomy*, vol. 230, no. 5, pp. 639–650, 2017.

[85] T. Delabastita, S. Bogaerts, and B. Vanwanseele, "Age-related changes in achilles tendon stiffness and impact on functional activities: a systematic review and meta-analysis," *Journal of Aging and Physical Activity*, vol. 27, no. 1, pp. 116–127, 2018.

[86] H. Zhao, Y. Ren, Y.-N. Wu, S. Q. Liu, and L.-Q. Zhang, "Ultrasonic evaluations of achilles tendon mechanical properties poststroke," *Journal of Applied Physiology*, vol. 106, no. 3, pp. 843–849, 2009.

[87] T. Muraoka, T. Muramatsu, T. Fukunaga, and H. Kanehisa, "Elastic properties of human achilles tendon are correlated to muscle strength," *Journal of Applied Physiology*, vol. 99, no. 2, pp. 665–669, 2005.

[88] J. Huang, K. Qin, C. Tang, Y. Zhu, C. S. Klein, Z. Zhang, and C. Liu, "Assessment of passive stiffness of medial and lateral heads of gastrocnemius muscle, achilles tendon, and plantar fascia at different ankle and knee positions using the myotonpro," *Med Sci Monit*, vol. 24, pp. 7570–7576, 2018.

[89] A. Monte, C. Maganaris, V. Baltzopoulos, and P. Zamparo, "The influence of achilles tendon mechanical behaviour on "apparent" efficiency during running at different speeds," *European Journal of Applied Physiology*, vol. 120, no. 11, pp. 2495–2505, 2020.

[90] C.-L. Kuo and G.-C. Hu, "Post-stroke spasticity: a review of epidemiology, pathophysiology, and treatments," *International Journal of Gerontology*, vol. 12, no. 4, pp. 280–284, 2018.

[91] J. Roots, G. S. Trajano, and D. Fontanarosa, "Ultrasound elastography in the assessment of post-stroke muscle stiffness: a systematic review," *Insights into imaging*, vol. 13, no. 1, pp. 1–14, 2022.

[92] A. Shamsoddini, S. Amirsalari, M.-T. Hollisaz, A. Rahimnia, and A. Khatibi-Aghda, "Management of spasticity in children with cerebral palsy," *Iranian journal of pediatrics*, vol. 24, no. 4, p. 345, 2014.

[93] R. L. Lieber and J. Fridén, "Muscle contracture and passive mechanics in cerebral palsy," *Journal of applied physiology*, vol. 126, no. 5, pp. 1492–1501, 2019.

[94] C. Boulard, R. Gross, V. Gautheron, and T. Lapole, "What causes increased passive stiffness of plantarflexor muscle–tendon unit in children with spastic cerebral palsy?" *European journal of applied physiology*, vol. 119, no. 10, pp. 2151–2165, 2019.

[95] J. T. Kalkhoven and M. L. Watsford, "The relationship between mechanical stiffness and athletic performance markers in sub-elite footballers," *Journal of Sports Sciences*, vol. 36, no. 9, pp. 1022–1029, 2018.

[96] M. Nakamura, R. Onuma, R. Kiyono, K. Yasaka, S. Sato, K. Yahata, T. Fukaya, and A. Konrad, "The acute and prolonged effects of different durations of foam rolling on range of motion, muscle stiffness, and muscle strength," *Journal of Sports Science & Medicine*, vol. 20, no. 1, p. 62, 2021.

[97] B. Skinner, R. Moss, and L. Hammond, "A systematic review and meta-analysis of the effects of foam rolling on range of motion, recovery and markers of athletic performance," *Journal of Bodywork and Movement Therapies*, vol. 24, no. 3, pp. 105–122, 2020.